Applied Thermal Engineering 277 (2025) 127104

Contents lists available at ScienceDirect

Applied Thermal Engineering

journal homepage: www.elsevier.com/locate/apthermeng

Research Paper

Resolving forward and inverse problems of rarefied gas heat transfer in an infrared detector cryochamber using physics-informed neural networks

Sang-Hyun Rhie [a], Eric Coatanéa [b], Sanga Lee [c], Wonjong Jung [a,*], Jeongsu Lee [d,*]

[a] Department of Mechanical, Smart, and Industrial Engineering, Gachon University, Seongnam 13120, South Korea
[b] Faculty of Engineering and Natural Sciences, Automation Technology and Mechanical Engineering, Tampere University, Tampere 33720, Finland
[c] Manufacturing AI Research Center, Korea Institute of Industrial Technology, Incheon 21999, South Korea
[d] Department of Mechanical Engineering, Kyung Hee University, Yongin 17104, South Korea

ARTICLE INFO

Keywords:
Rarefied gas conduction
Infrared detector cryochamber
Physics-informed neural networks
Inverse problem

ABSTRACT

This study presents a comprehensive analysis of rarefied heat transfer in cryogenic chambers with implications for infrared detector applications, using physics-informed neural networks (PINNs). Steady-state and transient heat transfer are analyzed to evaluate the steady cooling load and cooldown time as performance metrics in cryogenic chambers. We first developed a PINN-based framework to solve forward problems in rarefied gas heat transfer, presenting results by varying material properties and operating conditions such as thermal conductivity, emissivity, specific heat, rarefied gas pressure, and environmental temperature. The proposed framework is then extended to solve inverse problems, determining thermal conductivity and rarefied gas pressure based on operational requirements for steady cooling load and cooldown time in cryogenic chambers. Systematic analysis confirms that the proposed PINN-based framework successfully resolves both forward and inverse problems in rarefied gas heat transfer. We expect that the framework can be employed for the design of reliable cryogenic chambers and performance predictions under various environmental conditions.

1. Introduction

Infrared detector (IR) technology has various practical applications, including fire detection [1,2], robotics [3,4], industrial equipment [5,6], thermoelastic stress analysis [7,8], and medical diagnosis [9,10], owing to its ability to recognize long-wave electromagnetic radiation. One of the major areas in IR technology is photonic detectors, which are prized for their exceptional sensitivity and specificity to wavelengths around a few microns [6], enabling high-resolution imaging and accurate temperature measurements even in low-light environments [11]. However, to maintain these precise detection capabilities, photonic detectors must be cooled to temperatures below 80 K using specialized cryogenic chambers and cooling systems. A significant challenge within these cryogenic systems is efficiently insulating the IR detector to minimize heat transfer and cooling capacity leakage. Additionally, the IR detector must be quickly brought down to its operational temperature to ensure reliability under normal environmental conditions.

The challenging requirements of cryogenic cooling systems have prompted systematic investigations. One notable research direction focuses on the cooling characteristics of cryogenic chambers, aiming to propose optimal parameter designs and material properties in terms of cooling capacity [12]. These studies emphasize the importance of optimal design and operational conditions, particularly highlighting the critical role of gaseous conduction in influencing the cooling load [12–16]. Parametric analysis presents the effects of design parameters on both steady and transient cooling characteristics. Numerical models for predicting the behavior of an infrared cryochamber under transient conditions have been developed to design cooling strategies for specific scenarios such as target acquisition and tracking of projectile systems, thermal efficiency analysis, remote temperature sensing, and short-range wireless communication [17,18]. Furthermore, by incorporating radiation shields, the heat transfer in the cryogenic chamber becomes dominated by rarefied gas conduction, which significantly impacts the overall efficiency of the cryochamber [19].

In addition to chamber design, the development of cryogenic cooling systems, such as the Joule-Thomson cryocooler, is another primary focus of these investigations. The thermodynamic cycles of Joule-Thomson coolers have been extensively explored, with particular emphasis on optimizing the geometry of the cryocooler for enhanced performance in defense applications [20–24]. Numerical investigations into the steady-state thermal behavior of infrared detector cryochambers have

* Corresponding authors.
E-mail addresses: wonjongjung@gachon.ac.kr (W. Jung), leejeongsu@khu.ac.kr (J. Lee).

https://doi.org/10.1016/j.applthermaleng.2025.127104
Received 9 March 2025; Received in revised form 20 May 2025; Accepted 3 June 2025
Available online 5 June 2025
1359-4311/

Nomenclature

Fundamental physical quantities

a, b	coefficients of the linear cooling capacity model
A_c	cross-sectional area of the cryochamber (m^2)
ΔA_s	surface area of the cryochamber tip (m^2)
c	specific heat capacity (J/kg•K)
d_b	outer diameter of the cryochamber (m)
h, h_{total}	total heat transfer coefficient (W/m^2•K)
h_{gc}	heat transfer coefficient for gaseous conduction (W/m^2•K)
h_{local}	local heat transfer coefficient (W/m^2•K)
h_{rad}	heat transfer coefficient for radiative heat transfer (W/m^2•K)
k	thermal conductivity (W/m•K)
k_{air}	thermal conductivity of air (W/m•K)
k_0	thermal conductivity of air at room pressure and temperature (W/m•K)
Kn	Knudsen number
L	cryochamber length (m)
m	characteristic parameter in the fin equation
p	perimeter of the cold well (m)
P	gas pressure
P_{fm}	threshold pressure for free molecular flow
Q	heat flux (W/m^2)
Q_{rad}	radiative heat flux (W/m^2)
r_i	cold well radius (m)
r_o	vacuum vessel radius (m)
t	time (s)
T	temperature (K)
T_d	detector temperature (77 K)
T_m	mean temperature (K)
T_∞	ambient temperature or reference temperature (K)
ΔV	volume of the cryochamber tip (m^3)
x	position inside the cryochamber (m)
α	thermal diffusivity (m^2/s)
α_i	tapering rate of cold well radius
ε	emissivity (dimensionless)
ρ	density (kg/m^3)
σ	Stefan-Boltzmann constant
ω	weighting factor in the loss function

Acronyms

Adam	adaptive moment estimation (optimizer)
FDM	finite difference method
FEM	finite element method
IR	infrared
J-T	Joule-Thomson
L-BFGS-B	limited-memory Broyden-Fletcher-Goldfarb-Shanno with Box constraints (optimization algorithm)
MSE	mean squared error
ODE	ordinary differential equation
PDE	partial differential equation
PINNs	physics-informed neural networks

facilitated effective thermal analysis, thus improving the design of IR cryochambers [25]. Experimental investigations and thermophysical analysis of a Joule-Thomson cooler applicable to infrared imaging have been conducted [26], aiming to optimize the cooler's geometry for efficient performance [27].

The practical implementation of cryocooler systems requires systematic evaluation across various scenarios, including long-term durability, effective thermal analysis with integrated operational controls, and micro-scale applications. Modeling approaches that assess performance degradation and predict the operational lifetime of thermal devices under cyclic loading conditions provide valuable insights into the long-term reliability of cryogenic systems [28]. A related study on the steady-state thermal behavior of infrared detector cryochambers has contributed to the development of stable numerical models for effective thermal analysis [29]. Furthermore, the development and application of micro cryogenic coolers for infrared imaging have been highlighted, demonstrating their potential to significantly enhance the performance and miniaturization of IR detection systems [24].

The heat transfer analysis of a cryogenic chamber can be summarized by optimizing the following factors: 1) material properties such as thermal conductivity and emissivity, 2) design parameters such as the thickness and length of the cold well, and 3) operating conditions, including rarefied gas pressure. These parameters must be optimized to achieve the following objectives: minimizing steady cooling load and cooldown time. Mechanical analysis for this objective largely relies on numerical simulations that incorporate rarefied gas conduction in a vacuum vessel. Although the numerical simulation provides a thermodynamic assessment of the given cryogenic chamber, the optimized design must be iteratively updated based on parameters from previous experiments. Furthermore, the control system for cooling capability cannot be directly implemented based on the results of experimental simulations. The available experimental data are hard to incorporate into the numerical simulations. Therefore, this study aims to explore a complementary approach for analyzing the cryogenic chamber and rarefied gas conduction by employing the recently proposed strategy based on physics-informed neural networks (PINNs).

PINNs leverage deep learning architectures to incorporate physical laws into the neural networks' loss function. This capability enables the construction of solution curves for governing equations, data-conforming solution curves, and addresses inverse problems for parameter optimization [30]. Recent applications of PINNs have demonstrated their effectiveness in resolving coupled physics in thermal systems with spatially varying material properties, radiative boundaries, and heterogeneous media. For example, the ability of neural networks to approximate solutions to ordinary differential equations (ODEs) provides foundational insights supporting the application of PINNs in complex heat transfer problems [31]. These networks have also been used to solve conductive heat transfer partial differential equations (PDEs), with convective heat transfer PDEs included as boundary conditions, demonstrating improved efficiency and accuracy in modeling heat transfer processes [32]. In applications involving distinct material properties, PINNs have shown high precision in predicting temperature distributions, highlighting their effectiveness in heat conduction problems involving materials such as wood and steel [33]. The PINNs approach has also shown potential to partially replace traditional methods such as the finite element method (FEM), enhancing both accuracy and computational efficiency in heat conduction analyses [34]. Furthermore, a physics-informed hybrid learning framework has been introduced to improve predictions of critical heat flux in boiling systems. By embedding governing equations and domain constraints into a data-driven model, this approach enables more reliable safety margin evaluations across a broad range of operating conditions [35].

In addition, a major advantage of PINNs lies in their ability to address inverse problems in mechanical systems. An inverse problem involves directly optimizing input parameters to meet specific operational requirements. This capability is not readily achievable using conventional numerical simulations or experiments, as such approaches typically require numerous iterative simulations with varying inputs while monitoring the resulting target variables. For example, an inverse PINN architecture was proposed to estimate spatiotemporally varying thermal conductivity from sparse temperature measurements, achieving robust performance in reconstructing time-dependent conductivity profiles—even in the presence of noise and without prior knowledge of material distributions [36]. These studies collectively demonstrate that PINNs can not only approximate direct solutions but also infer hidden parameters from sparse or noisy observational data. Another notable implementation integrates PINNs with analytical heat conduction solutions to reconstruct three-dimensional temperature distributions from limited data, offering reliable inverse design capabilities under nonlinear boundary conditions [37].

Although increasing research has adopted PINNs for thermal engineering problems, the capability of PINNs to simulate and optimize rarefied gas heat transfer in cryogenic chambers has not yet been tested. This study develops PINNs for constructing the solution curve of heat transfer in a cryogenic chamber system. We then tested the capability of the developed PINNs for optimizing the design and operating conditions of the cryogenic chamber by considering inverse problems related to heat transfer. Consequently, design parameters including the thickness and length of the cold well, and the cooling capability of the cryocooler, are directly optimized based on the desired conditions of the cryogenic chamber such as steady cooling load and cooldown time.

In the following sections, we first present the heat transfer model of the cryogenic chamber. We then construct PINNs for resolving rarefied gas heat transfer in the cryogenic chamber in both steady and transient cases. The simulation results are discussed and validated in comparison with previous studies [12]. Finally, we integrate the PINNs model for steady and transient heat transfer into a single model, enabling the solution of inverse problems based on optimization. Example cases for the inverse design parameters optimization have been demonstrated.

2. Thermal modeling and PINN-based solutions

2.1. Modeling heat transfer in a cryogenic chamber

The thermal process in the cryogenic chamber is schematically illustrated in Fig. 1(a). An IR detector is placed onto the cold well and is encapsulated by the cryogenic chamber to minimize the leakage of cooling capacity. The inside of the chamber is vacuumed to reduce heat transfer. A J-T cryocooler is inserted into the cold vessel to maintain the IR detector at cryogenic temperatures, typically below 77 K. Cooling within the chamber occurs through the inner surfaces of the cold well, including the top surface and side walls. Consequently, three different heat transfer mechanisms are observed: 1) solid body conduction along the cold well, 2) radiative heat transfer, and 3) rarefied gas conduction from the cold well to the vacuum vessel. The main concerns with this system are the steady cooling load and the cooldown time. The steady cooling load refers to the necessary elimination of heat under nominal operating conditions, while the cooldown time corresponds to the response time from the environmental temperature to the operating temperature. The material properties of the cryogenic chamber are summarized in Table 1.

The steady-state heat transfer in cryogenic cooling systems focuses on solid body conduction, radiative heat transfer, and rarefied gas conduction. The steady-state heat transfer model is defined as follows [38]:

$$\frac{d^2T}{dx^2} - \frac{ph}{kA_c}(T - T_\infty) = 0 \tag{1}$$

where T is the temperature profile along the cold well, T_∞ is the base temperature corresponding to the ambient temperature, x is the axial position, p is the perimeter of the cold well, expressed as πd_b with the outer diameter d_b. A_c is the cross-sectional area, k is the thermal conductivity and h accounts for both rarefied gas conduction and radiative heat transfer. For transient analysis, the governing equation expands to:

$$\frac{\partial^2 T}{\partial x^2} - \frac{ph}{kA_c}(T - T_\infty) = \rho c \frac{\partial T}{\partial t} \tag{2}$$

where ρ is density, and c is specific heat capacity.

The thermal characteristics of the cryochamber are determined by the heat transfer coefficient h, which represents the leakage of cooling capacity. The total heat transfer to the cold well surface comprises both gaseous conduction and thermal radiation from the cryochamber vessel wall, represented as $h = h_{gc} + h_{rad}$. The heat transfer coefficients in the

Table 1
Material properties of the cryogenic chamber.

Elements	Material	Dimensions	Properties
Vacuum vessel	Stainless steel	Inner diameter = 25 mm	$\epsilon \approx 1$
Cold well	Borosilicate glass (outer surface electroplated with gold)	Outer diameter = 9 mm Thickness = 1 mm Length = 48 mm	$\epsilon = 0.02$ $\rho = 2640$ kg/m^3 $c = 800$ J/kg•K $k = 0.8$ W/m•K

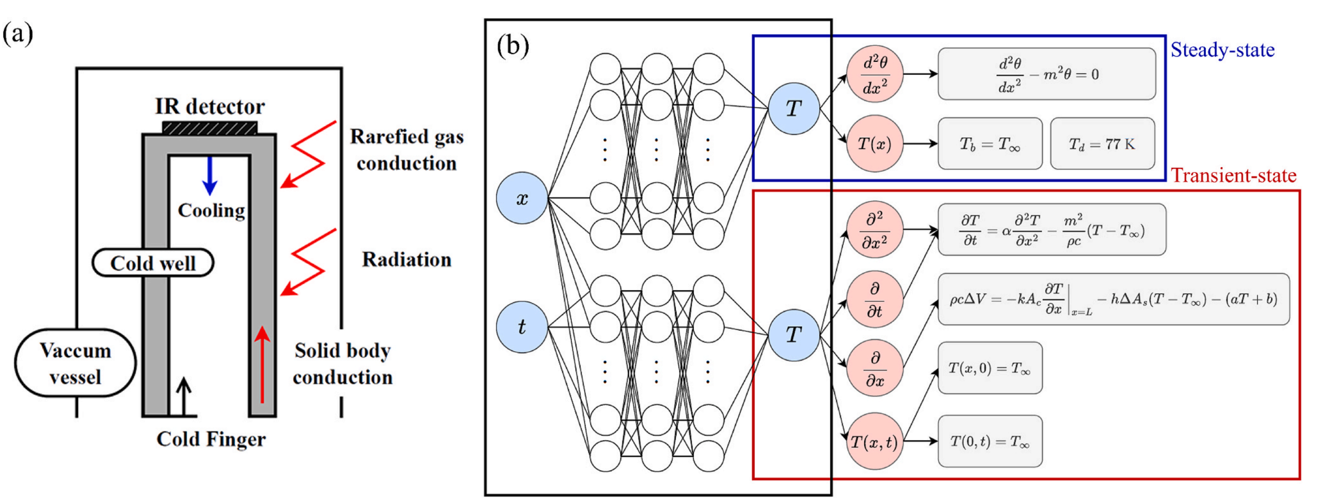

Fig. 1. (a) Schematic illustration of the heat transfer process in a cryogenic chamber where red arrows indicate heat transfer from solid conduction, rarefied gas conduction, and radiation, and a blue arrow denotes the cooling capability of the cryocooler. (b) Schematic illustration of PINN architecture for integrating both steady-state and transient-state heat transfer analysis. The diagram highlights the neural network structure, input variables x and t, and the respective governing equations and boundary conditions for each type of analysis.

cryochamber are discussed in Kim et al. [12], which is reproduced as follows. The heat transfer coefficient for gaseous conduction h_{gc} is represented, depending on the gas pressure Pa:

$$h_{gc} = \begin{cases} 1.48\cdot\mathbf{Pa} & \text{for } \mathbf{P} < 4\times10^{-4}\ \text{Torr} \\ \dfrac{1.48\cdot \text{Pa}}{1+0.34\cdot \text{Pa}} & \text{for } 4\times10^{-4}\ \text{Torr} \le P < 1\text{Torr} \\ 4.35 & \text{for } P \ge 1\text{Torr} \end{cases}$$

Further, the radiation heat transfer coefficient h_{rad} depends on the emissivity of the surfaces:

$$h_{rad} \approx 3\varepsilon\ [\mathrm{W/m^2K}] \tag{3}$$

This radiation heat transfer becomes significant in low-pressure or vacuum conditions where gaseous conduction is minimal, and radiative heat transfer dominates. The detailed derivation of h_{gc} and h_{rad} is referred to in section 2.3.

The boundary conditions for the models are constructed as follows: In the steady-state model, boundary conditions are $T_b = T_\infty$ which is temperature of the base identical to the ambient temperature and $T(L) = T_d$ where T_d is the detector temperature (77 K) and L the length of the cold well. For the transient-state model, initial condition $T(x,0) = T_\infty$ are set, and for boundary conditions $T(0,t) = T_\infty$ and energy balance at the tip of the cold well are applied. The energy balance at the tip of the cold well is given by Kim et al. [12]:

$$\rho c \Delta V \frac{\partial T}{\partial t} = -kA_c \frac{\partial T}{\partial x}\bigg|_{x=L} - h\Delta A_s (T - T_\infty) - (aT + b) \tag{4}$$

where ΔV and ΔA_s are the volume and the surface area of the tip, a and b are specific to each cryocooler model. In this work, we used $a = 0.039$ W/K and $b = -2$ W. This equation ensures the energy balance at the tip of the cold well, accounting for conductive, convective, and radiative heat transfer mechanisms.

2.2. Thermal conductance in rarefied gas conduction and radiative heat transfer

In low-pressure environments where the gas pressure ranges from 10^{-5} to 1 Torr, the molecular mean free path (λ) becomes comparable to the characteristic length scale (gap distance, l). This leads to the necessity of considering heat transfer under the rarefied gas regime. In this regime, heat conductance is described based on the Knudsen number (Kn), a dimensionless quantity defined as:

$$Kn = \lambda / l \tag{5}$$

This number classifies the heat transfer regimes such as free molecular flow ($Kn > 10$), transition regime ($10 > Kn > 0.1$), slip regime ($0.1 > Kn > 0.01$), and continuum regime ($Kn < 0.01$) [39].

Heat conductance for rarefied gases, denoted h_{gc}, is influenced by the gas pressure and falls into different regimes based on Kn and the molecular mean free path. At very low pressures, free molecular flow dominates, while higher pressures cause the gas to behave as a continuum.

The heat transfer coefficient for gaseous conduction depending on the gas pressure P (Pa), is described by three different formulas depending on the pressure regime. In the low-pressure regime where $P < 4\cdot10^{-4}$ Torr, molecular collisions with the chamber walls dominate heat transfer, and the conductance is directly proportional to the gas pressure:

$$h_{gc} = 1.48\cdot\text{Pa} \tag{6}$$

This linear relationship shows that as the pressure decreases, the mean free path increases, thus reducing conductance. In the intermediate pressure regime where $4\cdot10^{-4}$ Torr $\le P < 1$ Torr, heat is transferred through both molecular collisions and wall collisions. The conductance becomes nonlinear and can be expressed as:

$$h_{gc} = \frac{1.48\cdot\text{Pa}}{1 + 0.34\cdot\text{Pa}} \tag{7}$$

Nonlinear behavior arises due to the increasing role of intermolecular collisions as pressure increases. The term 1 +0.34 • Pa accounts for this transition [12,40]. At higher pressures, $P \ge 1$ Torr, the gas behaves like a continuous medium, and the thermal conductance is no longer sensitive to pressure changes, reaching a steady value:

$$h_{gc} = 4.35 \tag{8}$$

In this regime, molecular collisions dominate, and heat transfer is primarily governed by conduction, similar to the behavior in solid materials [40].

The molecular mean free path λ can be calculated using the following formula:

$$\lambda = \frac{k_B T}{\sqrt{2}\pi d^2 P} \tag{9}$$

where k_B is Boltzmann constant, T is the gas temperature, d is the effective molecular diameter of air (approximately 0.37 nm), and P is the gas pressure [41]. Free molecular flow dominates when the gas pressure is below the threshold P_{fm}, defined as:

$$P_{fm} \approx 4\cdot10^{-4}\ \text{Torr} \tag{10}$$

assuming a temperature range of 300 K to 77 K [12]. For pressures above this threshold, gas behavior transitions toward the continuum regime.

Radiative heat transfer occurs between surfaces at different temperatures, governed by the Stefan-Boltzmann law. The radiative heat flux between two surfaces can be written as:

$$Q_{rad} = \sigma\varepsilon\left(T_\infty^4 - T^4\right) \tag{11}$$

where σ is Stefan-Boltzmann constant, and ε is the emissivity of the cold well. For small temperature differences, the expression can be linearized using a first-order Taylor expansion around the mean temperature (T_m = 237K) [12]. The radiative thermal conductance h_{rad} can then be expressed as the ratio of the radiative heat flux to the temperature difference ΔT:

$$h_{rad} = \frac{Q_{rad}}{\Delta T} = 4\sigma\varepsilon T_m^3 \approx 3\varepsilon\ [\mathrm{W/m^2\cdot K}] \tag{12}$$

The approximation follows from typical values for T_m and simplifying the constants [12,42].

2.3. Constructing PINN for cryogenic chamber heat transfer analysis

Fig. 1(b) exhibits the schematic illustration of the PINNs for resolving heat transfer in a cryogenic chamber. The PINN architecture is constructed as an integration of two independent neural network architectures that address steady-state and transient heat transfers. Both models use spatial variables (x) as input, which are normalized to improve learning stability and performance. The transient-state model additionally includes temporal variables (t) as input, reflecting the time-dependent nature of the analysis. The PINN model consists of four fully connected layers, each with 20 neurons, and employs the tanh activation function. Training is conducted in two stages: first, the Adam optimizer with a learning rate of 0.01 facilitates rapid convergence, followed by the L-BFGS-B optimizer for fine-tuning and ensuring smooth loss reduction. This hybrid optimization approach effectively balances convergence speed and accuracy. Additionally, for the transient-state model, the architecture is enhanced by integrating an anti-derivative approximator based on Fourier series expansion after the dense layers [43], improving the model's ability to capture transient thermal behavior more accurately.

The last output layer provides the temperature prediction at each input point, scaled by a factor of 100 to match typical thermal gradients. The weights throughout the network are initialized using the Glorot normal initializer to prevent issues such as vanishing or exploding gradients during training. The tanh activation function maps real-valued inputs to the range [-1, 1], which is then scaled to the expected temperature range. For the sampling of collocation points, to accurately represent the spatial and temporal domains, the spatial variable (x) is discretized more finely near the boundaries: the initial 98 % of the domain is divided into 500 grid points, while the remaining area is divided into 1000. Similarly, the temporal variable is divided into three segments: the first 20 %, 30 %, and 50 %, each represented by 100 points, with finer resolution in the initial phase. This fine-grained discretization near the boundaries ensures higher resolution where it is most needed.

The loss functions include terms for differential equation constraints and boundary conditions to ensure physical accuracy. For the steady-state model, the governing equation (1) loss J_{ODE} and the boundary condition losses, with $J_{\mathrm{BC,\,start}}$ representing the loss at $x = 0$ and $J_{\mathrm{BC,\,end}}$ representing the loss at $x = L$, are calculated as follows: $J_{\mathrm{ODE}} = \frac{1}{n}\sum_{i=1}^{n}\left(\frac{d^2T}{dx^2} - \frac{ph}{kA_c}(T - T_\infty)\right)^2$, $J_{x=0} = \frac{1}{n}\sum_{i=1}^{n}(T(0) - T_\infty)^2$, $J_{x=L} = \frac{1}{n}\sum_{i=1}^{n}(T(L) - T_d)^2$. Thus, the total loss for the steady-state model is a weighted sum of these losses: $J_{\mathrm{Total}} = J_{\mathrm{ODE}} + \omega^2 \cdot J_{\mathrm{BC,\,start}} + \omega^2 \cdot J_{\mathrm{BC,\,end}}$ where $\omega = \frac{ph}{kA_c}$. This weighting approach prioritizes the accuracy of the boundary condition constraints slightly more than the differential equation.

In the transient-state model, the loss function includes several components to ensure the model accurately captures the dynamics of heat transfer over time. These components include the mean squared error (MSE) for the governing equation, initial conditions, and boundary conditions, including the energy balance equation at the tip grid ($x = L$). The governing equation loss, denoted as J_{PDE}, is calculated by evaluating the discrepancy between the time derivative of the temperature and the spatial derivative terms, captured by the following expression: $J_{\mathrm{PDE}} = \frac{1}{n}\sum_{i=1}^{n}\left(\frac{d^2T}{dx^2} - \frac{ph}{k^2A_c}(T - T_\infty) - \frac{\rho c}{k}\frac{\partial T}{\partial t}\right)^2$. This ensures that the transient heat conduction is modeled accurately according to the physical laws by considering both spatial and temporal changes in temperature, as well as the material properties of the system. Additionally, the total loss function J_{Total} incorporates other critical terms. J_{IC} accounts for the error in the initial condition. It ensures that the model's predicted temperature distribution at the initial time ($t = 0$) matches the known initial temperature distribution, which is T_∞. The loss function for the initial condition is expressed as: $J_{\mathrm{IC}} = \frac{1}{n}\sum_{i=1}^{n}(T(x,0) - T_\infty)^2$. For boundary conditions, $J_{x=0}$ and $J_{x=L}$ represent the losses at the base and the end of the cryochamber. These are defined as: $J_{x=0} = \frac{1}{n}\sum_{i=1}^{n}(T(0,t) - T_\infty)^2$, $J_{x=L} = \frac{1}{n}\sum_{i=1}^{n}\left(\rho c\Delta V\frac{\partial T}{\partial t} + kA_c\frac{\partial T}{\partial x}\Big|_{x=L} + h\Delta A_s(T - T_\infty) + (aT + b)\right)^2$. The total loss function is then expressed as: $J_{\mathrm{Total}} = \omega \cdot J_{\mathrm{PDE}} + J_{\mathrm{IC}} + J_{x=0} + \omega^2 \cdot J_{x=L}$. By using ω as the weight, the model emphasizes the importance of accurately capturing the transient dynamics of heat conduction and the critical boundary conditions. This unified weighting approach ensures that the most influential terms in the heat transfer process are prioritized, particularly in systems where the heat transfer coefficient plays a dominant role.

The training begins with the Adam optimizer [44] with a learning rate of 0.01 for a specified number of epochs. After the initial training via the Adam optimizer, the optimizer is switched to the L-BFGS-B method from SciPy [45]. This optimizer configuration was adopted after systematic experiments to achieve convergence in the PINNs, the details of which are demonstrated in Appendix A.

3. Resolving forward problems

3.1. Steady state analysis

Fig. 2 demonstrates the capability of the PINN solution in describing the steady state for the benchmark problem under the condition of rarefied gas pressure. The contour plot of the steady-state temperature profile in the cold well is shown in Fig. 2(a). This visualization highlights the spatial temperature gradients throughout the system, offering a clear view of how heat is distributed and managed within the cryogenic chamber. The training procedure begins with the Adam optimizer (depicted in blue), followed by the L-BFGS-B optimizer (depicted in yellow), as presented in Fig. 2(b). The sharp decrease in the loss curve confirms the convergence of the PINN solution. We compare the predicted temperature profile with the analytic solution of the fin equation, expressed as $T(x) = T_\infty - (T_\infty - T_d)\frac{\sinh mx}{\sinh mL}$, described by Eq. (1) in Fig. 1 (c). The prediction from the PINN solution corresponds well to the analytic solution, presenting $L1$ and $L2$ norm errors of 5.90×10^{-4} and 7.81×10^{-4}, respectively. The steady cooling load is then expressed by the conduction rate at the top surface where the IR detector is located, which is expressed as: $Q = kA_c\frac{dT}{dx}\Big|_{x=L}$.

We systematically evaluated the cooling characteristics of the cryochamber by varying the material properties of the chamber, such as thermal conductivity and emissivity, as well as the operating condition of the rarefied gas pressure, as shown in Fig. 3. First, thermal conductivity determines the solid body conduction through the cold well, which is the most dominant factor leading to the leakage of cooling capacity. We analyzed the steady cooling load by varying the thermal conductivity from 0.1 to 2, as shown in Fig. 3(a), when the rarefied gas pressure ranged from 10^{-4} to 1. The range of thermal conductivity corresponds to the material properties of heat-resistant glass (Table 1), which is adopted as an insulating material having structural strength. Higher conductivity results in an increased cooling load because materials with higher thermal conductivity significantly exacerbate cooling loss. This effect is more pronounced at higher gas pressures where convective heat transfer becomes more significant.

Furthermore, the influence of emissivity on the steady cooling load is discussed in Fig. 3(b). The emissivity of the surface has a limited impact on the steady cooling load within the range of emissivity from 10^{-2} to 10^{-1}, corresponding to the actual material properties of the cold well made of borosilicate glass [12]. However, the contribution of radiation heat transfer to the total steady cooling load is significant, especially when the inside of the cold well is maintained under a vacuum pressure below 10^{-3} Torr. In a highly vacuumed state (extremely low rarefied gas pressure), radiative heat transfer dominates the heat transfer from the cold well to the vacuum vessel. Thereby, radiative heat transfer is the second dominant factor leading to cooling leakage, following cooling loss via solid conduction.

As the steady cooling load varies insignificantly with the emissivity of the order of 10^{-2}, the overall cooling characteristics of the cryochamber system can be depicted in the plot of steady cooling load versus rarefied gas pressure as shown in Fig. 3(c). The different curves in Fig. 3 (c) highlight the variation in the thermal conductivity, from 0.2 to 1.1, of the cold well. As the gas pressure increases, the cooling load also rises, due to enhanced conduction in the presence of higher gas pressures, which contributes to the overall heat load that must be managed by the cooling system. Higher thermal conductivity leads to a greater cooling load across all pressures, reflecting the increased ability of the material to conduct heat. The combined effects of rarefied gas conduction and radiation are demonstrated in the temperature distribution plot in Fig. 3 (d), the total heat transfer coefficients approximately from 7.97×10^{-2} to 4.41. The temperature gradient becomes steeper as the heat transfer coefficient h increases, indicating more efficient heat removal from the cold well. The temperature profile severely deviates from the linear

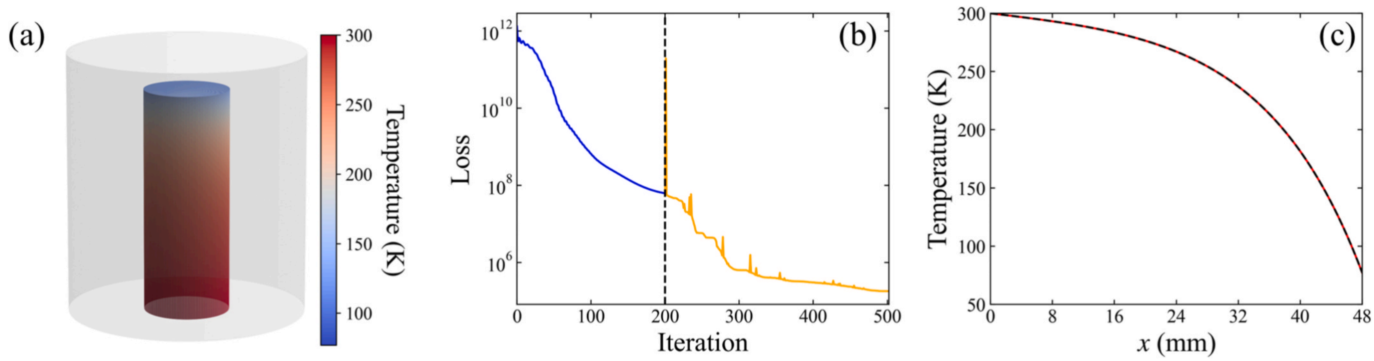

Fig. 2. Results of the steady-state analysis: (a) 3D visualization of the temperature distribution within the cold well, (b) loss reduction during training with Adam and L-BFGS-B optimizers, and (c) temperature profile along the cold well compared with the analytical solution.

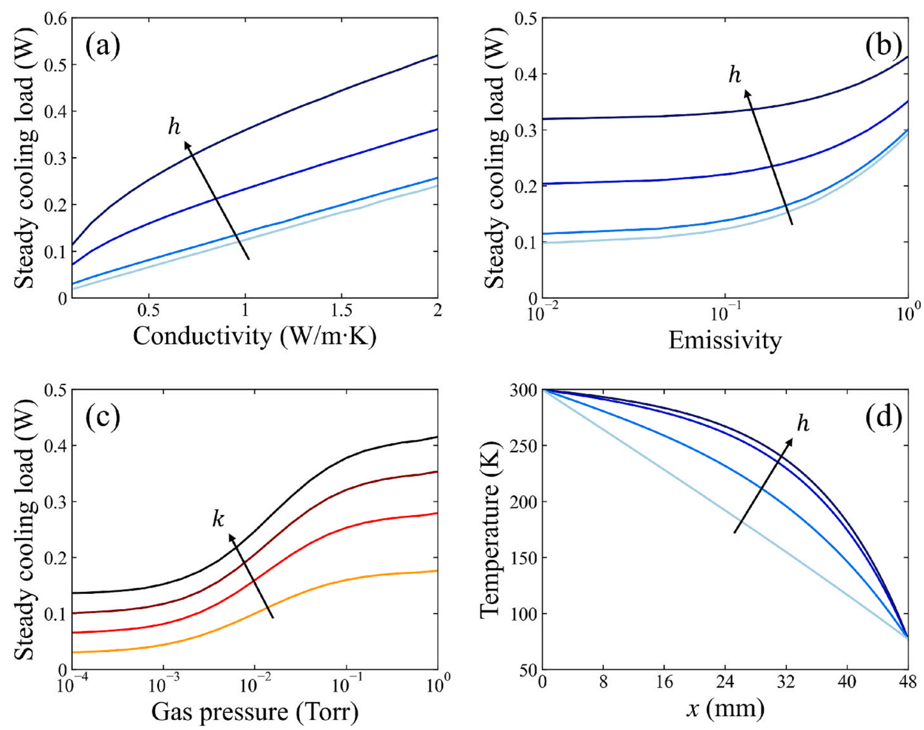

Fig. 3. Effects of material properties (conductivity and emissivity) and operating conditions (rarefied gas pressure) on the steady cooling load. Steady cooling load versus (a) conductivity, (b) emissivity, and (c) rarefied gas pressure. (d) Temperature distribution along the cold well, with blue indicating the combined effects of rarefied gas conduction and radiation on the heat transfer coefficient.

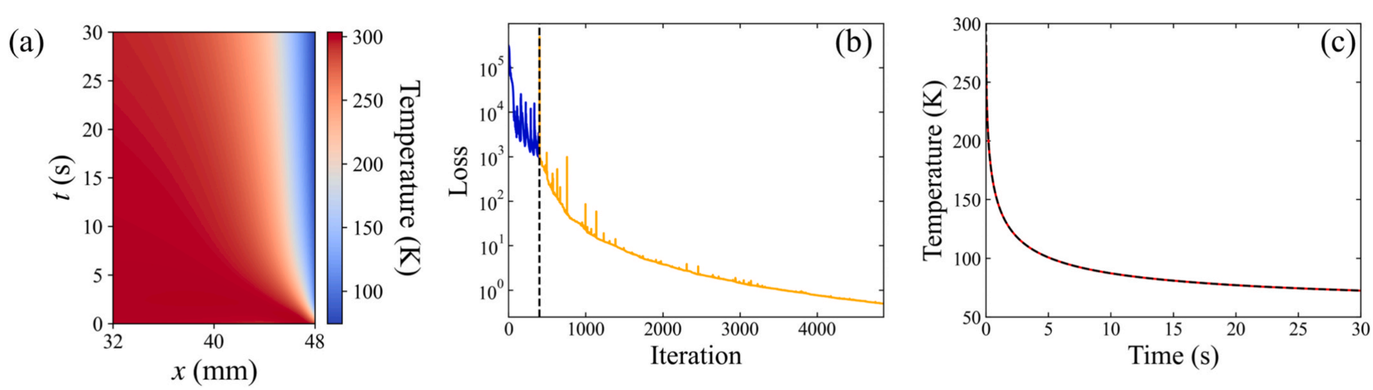

Fig. 4. Results of the transient-state analysis: (a) temperature distribution over time along the cold well, (b) loss convergence during training with Adam and L-BFGS-B optimizers, and (c) temperature evolution at the tip compared with the analytic solution.

trend as the heat transfer coefficient increases.

3.2. Transient state analysis

Next, we considered the transient-state heat transfer in a cryo-chamber as described by Eq. (2), the temporal variation of heat capacity influences the cooldown time of the IR detector, and the linearized cooling capacity model is represented by $Q = aT(x = L, t) + b$. To validate the PINN solution, we first examined the trivial case in which the side wall of the cold well is adiabatic (i.e., $h = 0$), for which analytic solutions are available [46]. The solutions are given by:

$$T_s = \left(T_\infty + \frac{b}{a}\right)\exp\left(\left(\frac{a}{kA_c}\right)^2 \alpha t\right)\operatorname{erfc}\left(\frac{a}{kA_c}\sqrt{\alpha t}\right) - \frac{b}{a} \tag{13}$$

Fig. 4(a) presents the predicted contour plot for the temporal variation of the temperature profile over x, and Fig. 4(b) shows the convergence of the PINN solution. Fig. 4(b) illustrates how the Adam optimizer effectively reduced the loss during the initial training phase, with further optimization achieved through the L-BFGS-B optimizer, as indicated by continued loss reduction over more iterations. By comparing the PINN predictions with the analytic solutions (Fig. 4(c)), we can assess the suitability of the PINN approach for solving heat transfer problems in cryogenic cooling systems. These experiments confirm that the PINN model produces accurate solutions compared to the analytic solutions, capturing the transient behavior effectively.

The transient cooling characteristics of the cryogenic chamber are illustrated in Fig. 5(a) and (b). In Fig. 5(a), the temperature distribution is shown for the cold well over time, focusing on specific intervals along the axial length of 32 to 48 mm. This visualization spans from 6 s to 30 s, starting from a nominal operating temperature of 300 K. By capturing discrete snapshots at various points along the cold well, Fig. 5(a) highlights how the temperature gradient and the associated cooling front propagate through the system as time progresses. Meanwhile, Fig. 5(b) concentrates on the cooldown of the infrared (IR) detector located at the tip of the cold well ($x = L$), offering insight into the final stage of the cooling process. The temperature evolution at this critical location reveals that the IR detector typically reaches the desired operating temperature between approximately 27.65 and 27.85 s. We note that the experimental results agree with the test data from cryochamber experiments (GEC-Marconi type 66RPW/T2982) of corresponding dimensions reported in previous research [12].

Additionally, we investigated the cooling characteristics of a cryogenic chamber by varying its material properties and operating conditions, as shown in Fig. 5(c–h). The influence of the chamber's material properties—thermal conductivity, density, and specific heat capacity—on cooldown time was examined under rarefied gas pressures of 10^{-4}, 10^{-2}, and 100 Torr, as illustrated in Fig. 5(c–e). Among these properties, thermal conductivity showed the most critical influence on cooldown time (Fig. 5(c)). Specifically, the cooldown time increased from about 15 s to 55 s as the thermal conductivity rose from 0.2 W/m·K to 1.4 W/m·K. Higher material densities also significantly lengthened the

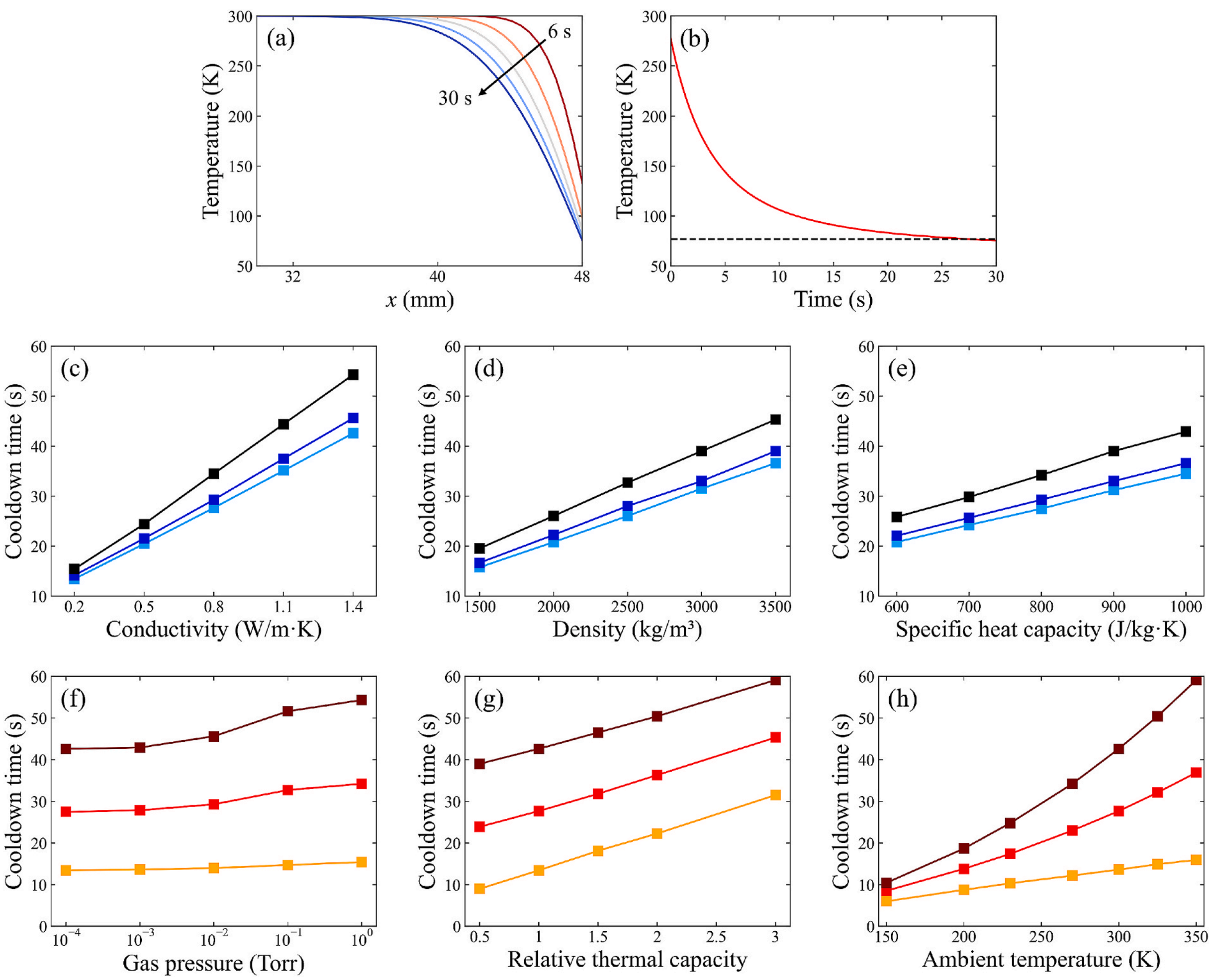

Fig. 5. Effects of material properties (conductivity, density, and specific heat capacity) and operating conditions (rarefied gas pressure, relative thermal capacity, and ambient temperature) on the cooldown time. Cooldown time versus (a) conductivity, (b) density, (c) specific heat capacity, (d) rarefied gas pressure, (e) relative thermal capacity, and (f) ambient temperature.

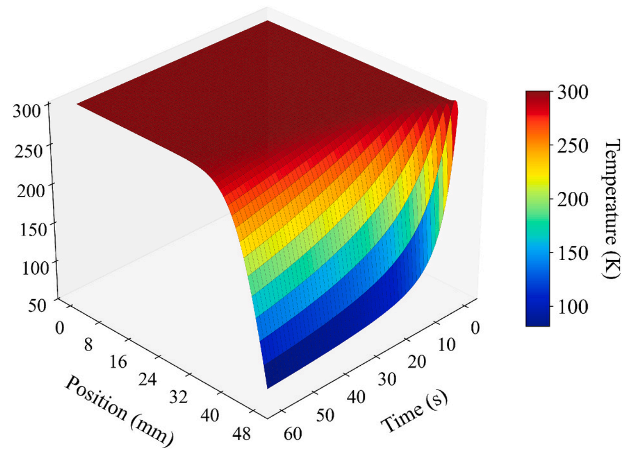

Fig. 6. 3D contour plot of temperature as a function of position and time.

cooldown period, because denser materials possess greater thermal mass and therefore retain heat for longer. This effect was especially pronounced at higher gas pressures, underscoring the importance of selecting lower-density materials for systems that require rapid cooling (Fig. 5(d)). Fig. 5(e) demonstrates that an increase in specific heat capacity similarly prolongs the cooldown time. Materials with higher specific heat capacity store more thermal energy, slowing the overall cooling process. Taken together, these findings highlight the trade-offs among thermal conductivity, density, and specific heat capacity, emphasizing the need for careful selection of material properties in cryogenic applications.

The influence of operating conditions, including gas pressure, the thermal capacity of the detector, and ambient temperature, on cooldown time has been investigated in Fig. 5(f–h) under varying thermal conductivities of 0.2, 0.8, and 1.4 W/m·K. Fig. 5(f) demonstrates that cooldown time increases with gas pressure, as higher pressures reduce the effectiveness of conductive heat transfer. The effects of the thermal capacity of the IR detector on cooldown time were then examined, with a relative thermal capacity of 1 corresponding to a reference condition where the top plate has a thickness of 1 mm. Higher relative thermal capacity leads to longer cooldown times due to the increased energy required for cooling. Fig. 5(h) highlights the relationship between ambient temperature and cooldown time, showing that higher ambient temperatures slow the cooling process. Across all these factors, materials with higher thermal conductivity consistently exhibit better cooling performance, underscoring the importance of optimizing both material properties and environmental conditions in cryogenic systems.

Finally, we present the temperature distribution over time and position for the transient cooling state of the cryogenic chamber, as shown in Fig. 6. The three-dimensional surface plot illustrates how the temperature decreases from an initial value of 300 K at $t = 0$ to a lower steady-state value over time. The horizontal axis represents the position along the system, while the depth axis represents time. The color gradient indicates the temperature, with red representing higher temperatures and blue representing lower temperatures. Initially, the entire system is at a uniform temperature of 300 K. As time progresses, the cooling effect from the cold tip ($x = L$) propagates along with the position axis, leading to a gradual decrease in temperature. This visualization effectively captures the transient behavior of the system, the temperature dynamically evolves in both space and time until equilibrium is reached. Such a representation is crucial for understanding heat transfer mechanisms and for designing systems that require precise thermal management.

Table 2
Mechanical properties of possible cryochamber materials.

Materials	Conductivity (W/m•K)	Density (kg/m^3)	Specific heat capacity (J/kg•K)	Emissivity
Stainless steel (304)	16.0	8000	500	0.30
Copper oxide coating	33.0	6400	380	0.75
Titanium	21.9	4500	523	0.40
CFRP	25.0	1600	800	0.70
Alumina	30.0	3960	880	0.25

3.3. Impact of material properties on cooling performance

Although cooling characteristics are among the most critical considerations when designing a cryogenic chamber, structural robustness and shock resistance are equally essential for applications in military and extreme environments. These additional requirements ensure that the cryogenic chamber can withstand harsh conditions, such as vibrations, impacts, and sudden temperature changes, without compromising its performance. To address this, we further investigated how the cooling characteristics vary depending on the cold well materials under different rarefied pressures for a range of materials, including stainless steel (304), copper oxide coating, titanium, carbon fiber reinforced plastic (CFRP), and alumina. The mechanical properties of examined materials are summarized in Table 2.

Fig. 7(a) and (b) illustrate the steady cooling load and cooldown time, respectively, for a range of materials. Alumina and CFRP, which exhibit higher steady cooling loads, tend to have significantly longer cooldown times due to their higher thermal mass or lower thermal conductivity. Materials with high thermal mass retain more heat energy, slowing the cooling process even if they place greater demands on the cooling system. Similarly, low thermal conductivity reduces the rate of heat dissipation, further extending the cooldown duration. These results highlight that a low steady cooling load does not necessarily correlate with faster cooling. Therefore, both steady cooling load and cooldown time must be carefully considered when selecting materials to ensure optimal performance in cryogenic applications, especially for systems operating in demanding environments. It is worth noting that further discussions on the optimal materials for the cryogenic chamber, considering structural and reliability requirements, are beyond the scope of this work, which focuses specifically on thermal characteristics.

Investigations into variations in material properties extend the discussion of cryochamber design to account for practical operational requirements. In this study, three additional scenarios are examined. The first scenario considers the mechanical strength of the cryochamber under conditions of high vibration and mechanical stress, requiring materials with higher thermal conductivity to ensure structural stability. The second scenario evaluates the impact of increased surface emissivity to assess the relative importance of radiative heat transfer compared to rarefied gas conduction. The third scenario involves an extreme vacuum environment, representing an ultra-low rarefied gas pressure achieved through advanced vacuum devices. The material properties used in each scenario are summarized in Table 2.

A controlled sensitivity analysis was conducted by varying one parameter at a time—thermal conductivity, surface emissivity, or rarefied gas pressure—while keeping the others constant as summarized in Table 3. Fig. 8(a) and (b) illustrate the resulting temperature distributions for steady-state and transient conditions, respectively. In the steady-state case shown in Fig. 8(a), higher thermal conductivity results in a smoother axial temperature gradient along the cold well due to improved heat transport. An increase in surface emissivity enhances radiative losses, slightly lowering the temperature near the detector. In

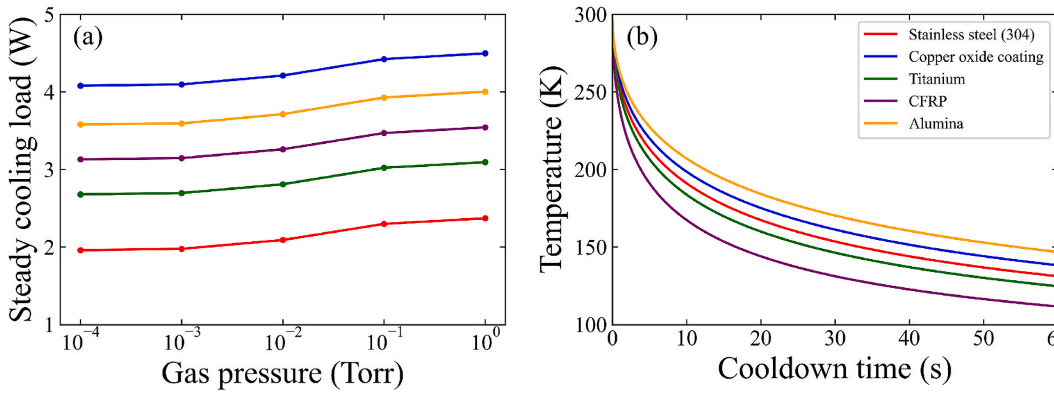

Fig. 7. Variations in steady cooling load and cool down time by cryochamber materials.

Table 3
Simulation cases with varying thermal conductivity, surface emissivity, and rarefied gas pressure for evaluating their influence on transient heat transfer behavior.

	Conductivity (W/m•K)	Emissivity	Pressure(Torr)
Case 1 (Reference)	0.8	0.02	1
Case 2 (High conductivity)	2.4	0.02	1
Case 3 (High emissivity)	0.8	0.60	1
Case 4 (Low pressure)	0.8	0.02	10^{-4}

contrast, reducing the rarefied gas pressure significantly lowers the overall heat transfer coefficient, steepening the temperature gradient and raising the upstream temperature.

The transient response, shown in Fig. 8(b), exhibits different behavior. Materials with higher thermal conductivity exhibit greater thermal inertia, which slows the cooling rate due to their higher heat capacity. Conversely, increased surface emissivity and lower gas pressure both accelerate cooling by enhancing heat rejection, reducing the time required to reach the target cryogenic temperature at the detector tip. These findings underscore the complex interplay between material properties and environmental conditions. Notably, gas pressure exerts a dominant influence under vacuum-like conditions where rarefied gas conduction becomes the limiting factor. Surface emissivity primarily affects local radiative losses at the warm end, while thermal conductivity dictates the rate of internal heat diffusion. Together, these results highlight the necessity of multi-parameter optimization in cryogenic system design, as performance metrics such as steady-state cooling load and cooldown time may respond in opposing ways to a single material change.

4. Configuring inverse problems for direct cryochamber design optimization

One of the major advantages of PINNs is their ability to address inverse problems [47–49] where the parameters of a given system can be directly adjusted to achieve desired target output variables. In this study, we apply the inverse problem configuration to the developed PINNs solution for rarefied gas heat transfer. The target variables for the cryogenic chamber are the steady cooling load and cooldown time. Thus, the primary objective of the inverse problem is to determine the parameters of the cryogenic chamber, including material properties and operating conditions, that meet the requirements for steady cooling load and cooldown time.

The key design parameter for the cryogenic chamber is the thermal conductivity k of the vessel material, which significantly influences the cooling characteristics. Additionally, the heat transfer coefficient h of the cold well, determined by factors such as the vessel's dimensions, surface emissivity, and rarefied gas pressure, plays a critical role in the overall system performance. Consequently, the inverse problem involves tuning the thermal conductivity and heat transfer coefficient to achieve the desired values for steady cooling load and cooldown time. This optimization process balances material properties, geometric configurations, and operational conditions to meet predefined targets, ensuring the cryogenic system's reliability and efficiency under practical conditions.

The configuration of the inverse problem to achieve the targeted steady and transient thermal characteristics is illustrated in Fig. 9. In this approach, parameters such as thermal conductivity and heat transfer

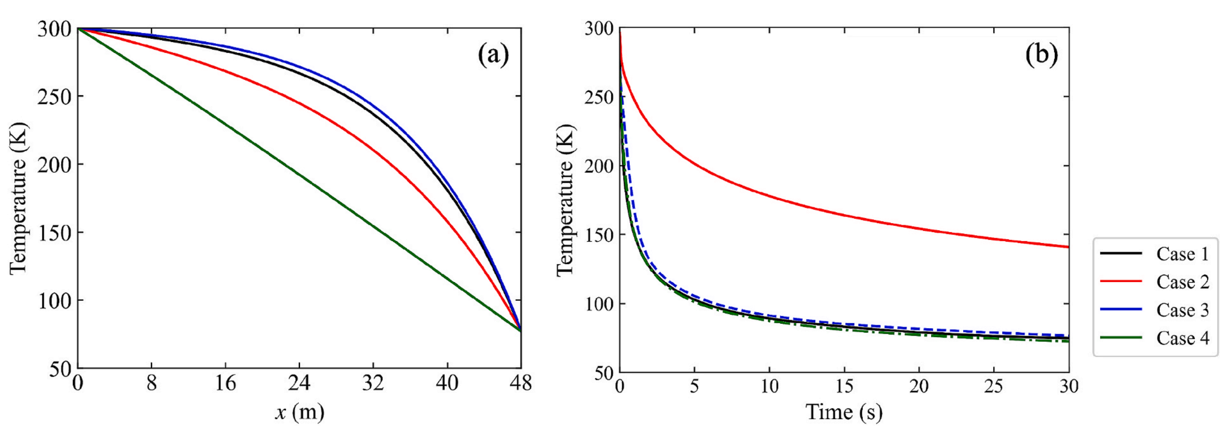

Fig. 8. (a) Steady-state temperature distribution along the cold well for different parameter variations: increased thermal conductivity, increased surface emissivity, and reduced gas pressure. (b) Transient temperature evolution at the detector end, showing cooldown behavior under the same parameter variations.

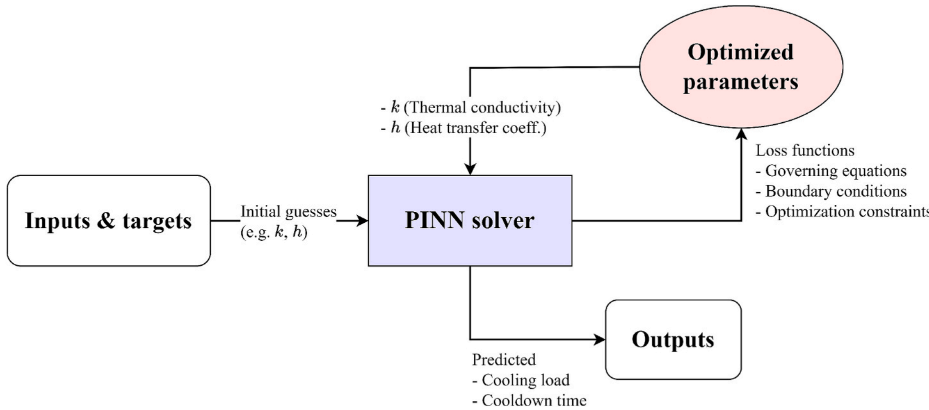

Fig. 9. Schematic illustration of the configured inverse problem-solving PINN solver for cryochamber design optimization.

coefficient are treated as trainable variables within the PINN-based inverse problem solver. To ensure the desired outcomes, specific loss functions are introduced to impose constraints on the steady cooling load and cooldown time. The cooling load is directly computed by summing the conductive heat flux at the tip ($x = L$) and a heat generation in the detector: $Q = -kA_c m(T_d - T_\infty)\frac{\cosh mL}{\sinh mL} + Q_{bias}$. The loss function for the steady cooling load is defined as $J_{steady} = \frac{1}{n}\sum_{i=1}^{n}(Q_{PINN} - Q_{target})^2$. This loss ensures that the predicted cooling load matches the desired target value. For the transient state, the cooldown time is constrained by evaluating the time it takes for the temperature at $x = L$ to reach the target temperature T_d. The loss function for the cooldown time is defined as $J_{transient} = \frac{1}{n}\sum_{i=1}^{n}(t_{PINN} - t_{target})^2$. Here, t_{PINN} is the predicted cooldown time, and t_{target} is the desired target time.

The results of resolving the inverse problem are demonstrated in Figs. 10 and 11, corresponding to the steady-state and transient state, respectively. We first resolve the inverse problem to determine the thermal conductivity of the vessel by varying the requirements for steady cooling load, as shown in Fig. 10(a) and (b). Fig. 10(a) verifies that the PINN-based solver successfully optimizes the thermal conductivity to achieve the desired steady cooling load, as indicated by the black line in the forward simulation results. The directly optimized condition exhibits good agreement with these results, as depicted by the range plot in blue, which represents the min–max range of the predictions from ten repetitive optimization trials. The optimized thermal conductivity aligns closely with the forward problem results, as illustrated in Fig. 10(b), which shows the relationship between target cooling load and thermal conductivity. Furthermore, the rarefied gas pressure, a crucial operating condition, can also be directly optimized using the presented PINN-based solver. This is demonstrated in Fig. 10(c), which plots gas pressure against the target cooling load. The black line represents the forward simulation results, while the green error bars indicate the optimized gas pressure conditions for achieving the target steady cooling load. These results confirm the capability of the PINN-based solver to directly optimize material properties and operating conditions of the cold well to satisfy the requirements for steady cooling load.

For the transient-state case, the temporal evolution of the temperature profile is solved under dynamic conditions, with the requirement that the cooldown time reaches a temperature of 77 K at the cold well tip. The results are presented in Fig. 11 where the cooldown time for the inversely determined conductivity condition is compared to the target cooldown time in Fig. 11(a). The inverse solver accurately captures the thermal conductivity that satisfies the target cooldown time, as shown in Fig. 11(b), which presents the plot of conductivity versus cooldown time. Overall, the inverse problem framework builds upon the established forward problem methodology, leveraging the same governing equations and optimization techniques while extending the solution to identify optimal parameters for achieving target thermal performance metrics. This unified approach enhances the applicability of PINNs for solving complex heat transfer problems in cryogenic systems.

5. Effect of axial geometry on heat transfer coefficients

The practical application of an IR detector cryochamber involves additional geometric complexities, such as a tapered cold well, as schematically illustrated in Fig. 12. This tapered geometry offers several advantages, including enhanced structural stability, improved thermal insulation, and better optical access [50]. However, it also introduces a more complex heat transfer process due to spatial variations along the x-axis. These variations significantly affect both conductive and radiative heat transfer characteristics, as they alter the cross-sectional area and

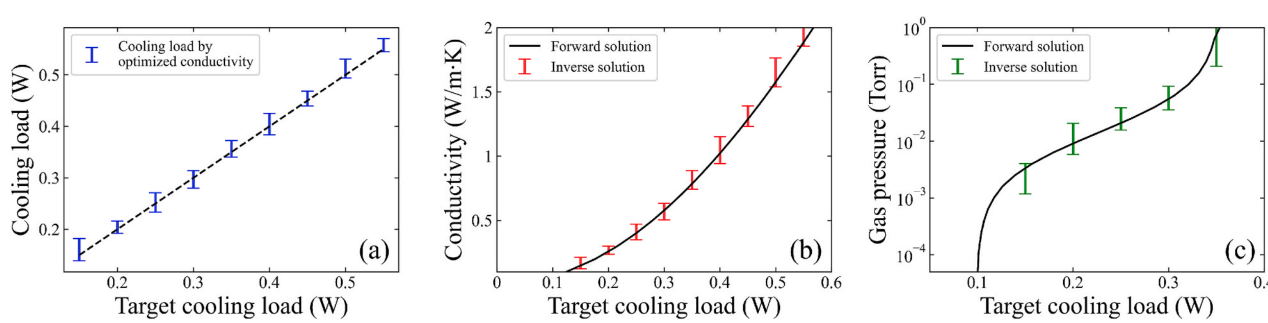

Fig. 10. Results of the inverse problem for optimizing thermal conductivity and rarefied gas pressure by varying the requirements for steady cooling load. (a) Verification of meeting the cooling load requirement. Directly obtained (b) thermal conductivity and (c) cooling load for various target cooling loads. The black line corresponds to the solution curve for thermal conductivity and rarefied gas pressure versus cooling load. The red and green lines indicate the optimized thermal conductivity and gas pressure, respectively. Error bars represent the range of predictions over ten repeated trials.

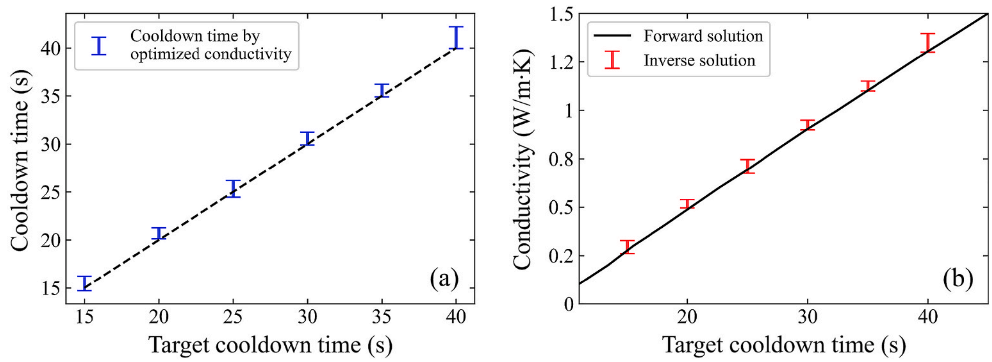

Fig. 11. Results of the inverse problem for optimizing thermal conductivity by varying the requirements for cooldown time. (a) Verification of meeting the cooldown time requirement. (b) Directly obtained thermal conductivity for various target cooldown times. The black line represents the solution curve for thermal conductivity versus cooling load, while the blue and red lines indicate the results of the inverse problems. Error bars represent the prediction ranges over ten repeated trials.

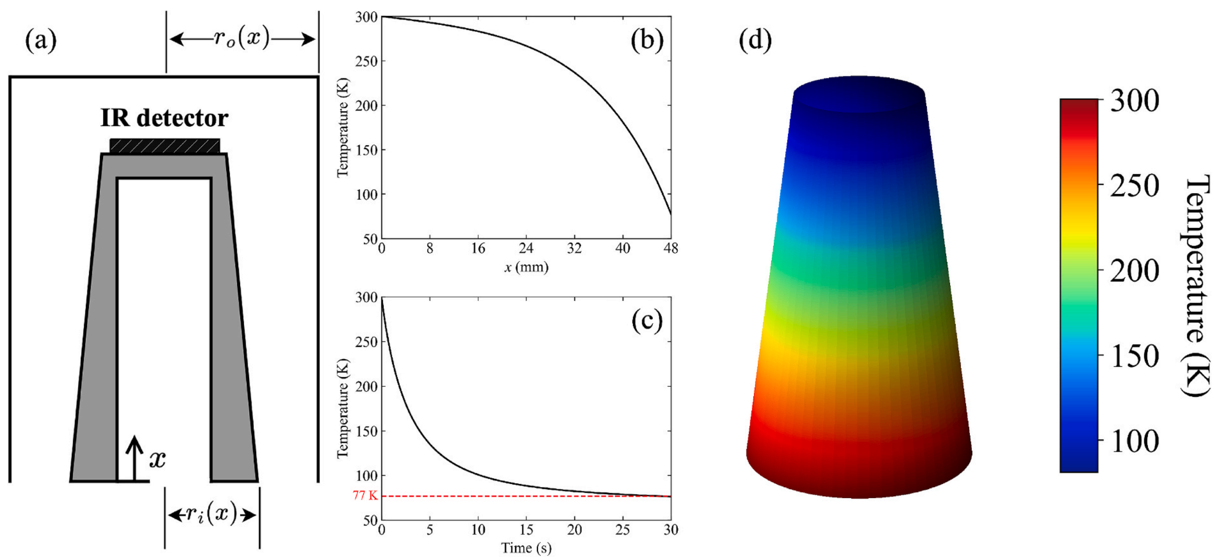

Fig. 12. (a) Schematic of the tapered cryogenic chamber where the inner radius r_i decreases along the axial direction, forming a conical geometry. The outer diameter r_o is held constant. The tapering structure introduces spatial variation in the gas gap and surface area, which affects both rarefied gas conduction and radiative heat transfer coefficient. (b) Steady-state temperature distribution along the cold well. (c) Temporal evolution of the temperature at the tip of the cold well, with a dashed line indicating the target detector temperature of 77 K. (d) Three-dimensional visualization of the temperature field within the tapered geometry under steady-state conditions, highlighting the radial symmetry and cooling behavior.

surface-to-volume ratio along the axial direction. This section investigates how such geometric changes influence the overall cooling performance.

The cryochamber geometry is defined by a fixed outer radius and a linearly tapering inner radius, resulting in an axial variation described by equation $r_i(x) = r_{i0} - \alpha_i x$. In typical cryochamber designs, the variation in the inner radius is relatively small compared to the absolute values of the inner and outer radii. As a result, we assume that the local heat transfer coefficient, h_{local}, can be reasonably approximated based on the instantaneous local values of $r_{\text{i}}(x)$ and r_{o}, while neglecting higher-order effects from axial gradients such as lateral conduction or radiation view factor changes.

Additionally, the tapered structure alters the rarefied gas conduction pathway, deviating from the classical heat transfer between concentric cylinders. The local heat transfer coefficients, accounting for geometric variations, are determined as follows. The rarefied gas conduction coefficient is given by

$$h_{\text{gc}}(x, T(x)) = \frac{k_{\text{air}}(x, T(x))}{r_i(x)\cdot\ln(r_o/r_i(x))} \tag{14}$$

where $k_{\text{air}}(x)$ is the local effective thermal conductivity of air [51]. This local effective thermal conductivity is expressed as

$$k_{\text{air}}(x, T(x)) = \frac{k_0}{1 + \dfrac{7.6\times10^{-5}}{P\cdot\left(\dfrac{r_o - r_i(x)}{T_m(x)}\right)}} \tag{15}$$

With $k_0 = 0.02643$ W/m•K, P is the local pressure (in bar), and $T_m(x)$ the mean gas temperature. The mean gas temperature is defined as based on the local temperature $T(x)$ and the ambient temperature T_∞ at corresponding x section. The radiative heat transfer coefficient is defined by

$$h_{\text{rad}}(x) = \sigma\varepsilon\left(T_\infty^2 + T(x)^2\right)(T_\infty + T(x)) \tag{16}$$

based on the linearized Stefan-Boltzmann approximation based on Eqs.10 and 11.

The total heat transfer coefficient is expressed as $h_{\text{total}}(x, T(x)) = h_{\text{gc}}(x, T(x)) + h_{\text{rad}}(x, T(x))$. This formulation captures the position- and temperature-dependent thermal behavior of the tapered configuration while maintaining a tractable modeling approach, as described by Eqs. (14) and (16). These expressions reflect both the pressure-sensitive characteristics of rarefied gas conduction and the nonlinear nature of radiative heat transfer near the cold well walls. However, the local heat transfer coefficients themselves are functions of the temperature distribution, resulting in a coupled nonlinear heat transfer problem. Since both h_{gc} and h_{rad} depend on the local temperature, they must be evaluated self-consistently as part of the solution to the governing heat transfer equation. Solving this equation yields the temperature profile, which in turn determines the local heat transfer coefficients, ensuring that they satisfy both the physical constraints and the thermal boundary conditions described below.

We first present the simulation results for steady-state heat transfer, as shown in Fig. 13, by varying the rarefied gas pressure. The heat transfer process exhibits characteristic transitions, which are reflected in the spatial distribution of the local heat transfer coefficients. The gas conduction coefficient h_{gc} decreases significantly as the chamber pressure drops from 1 Torr to 10^{-4} Torr. At 1 Torr, h_{gc} exceeds 4.25 W/m^2·K, dominating the overall heat transfer as shown in Fig. 13(a). However, as the pressure decreases, molecular collisions become increasingly rare, causing the effective thermal conductivity of the gas to decline sharply—falling below 0.03 W/m^2·K at 10^{-4} Torr. In contrast, the radiative component h_{rad} remains largely independent of pressure but exhibits spatial variation due to the temperature gradient along the cold well. Specifically, h_{rad} decreases monotonically from the warm entrance to the cryogenically cooled tip, contributing more significantly near the inlet and less at the coldest end.

At high pressures, such as 1 Torr, the total coefficient closely follows the behavior of h_{gc}, with minimal contribution from radiation. As the pressure decreases to 0.1 Torr, conduction still dominates; however, the relative contribution from radiation becomes more noticeable—particularly near the entrance where the temperature is higher, as shown in Fig. 13(b). A distinct transition occurs around 10^{-3} Torr (Fig. 13(c)) where gas conduction and radiation reach comparable magnitudes across different spatial regions. Specifically, radiation dominates near the warm entrance, while gas conduction becomes more significant toward the cold end. This opposing behavior results in a U-shaped profile for the total heat transfer coefficient, with a minimum occurring at mid-length and increasing values toward both ends. This regime marks a crossover zone in which neither mechanism is negligible, requiring accurate resolution of both contributions for realistic thermal modeling.

Further decreasing rarefied gas pressure (as shown in Fig. 13(d), corresponding to 10^{-4} Torr), the total heat transfer becomes increasingly dominated by radiation, as gas conduction drops below 0.03 W/m^2·K. In this deep-vacuum regime, the total coefficient decreases monotonically along the axial direction, closely following the spatial trend of h_{rad}. The resulting smooth profile indicates that radiation is the sole significant contributor to thermal losses under these conditions. This marks a clear transition from conduction-dominated to radiation-dominated heat transfer behavior as pressure decreases. Accurately capturing this shift is essential for designing cryochambers operating under varying vacuum levels and for selecting appropriate cooling strategies.

The transient cooling process additionally introduces time dependence into the local heat transfer coefficient, which is governed by the temporal evolution of the temperature profile. The variation of heat transfer coefficients over time exhibits characteristic transitions depending on the rarefied gas pressure, corresponding to the steady-state behavior shown in Fig. 14. At high pressures (e.g., Fig. 14(a), 1 Torr), the rarefied gas temperature dominates, $h_{gc}(x = L, t, T(x, t))$ increases sharply and stabilizes, while $h_{rad}(x = L, t, T(x, t))$ decreases rapidly dure to the strong early temperature gradient. The total heat transfer coefficient stabilizes quickly, indicating rapid energy dissipation at the cold tip. In constrast, at intermediate pressures (e.g., Fig. 14 (b) and (c)), the interplay between conduction and radiation is more balanced. The total coefficient increases more gradually, highlighting a transitional regime where more mechanisms significantly contribute at different stages of cooling.

At very low pressures (e.g., Fig. 14(d), 10^{-4} Torr), conduction is

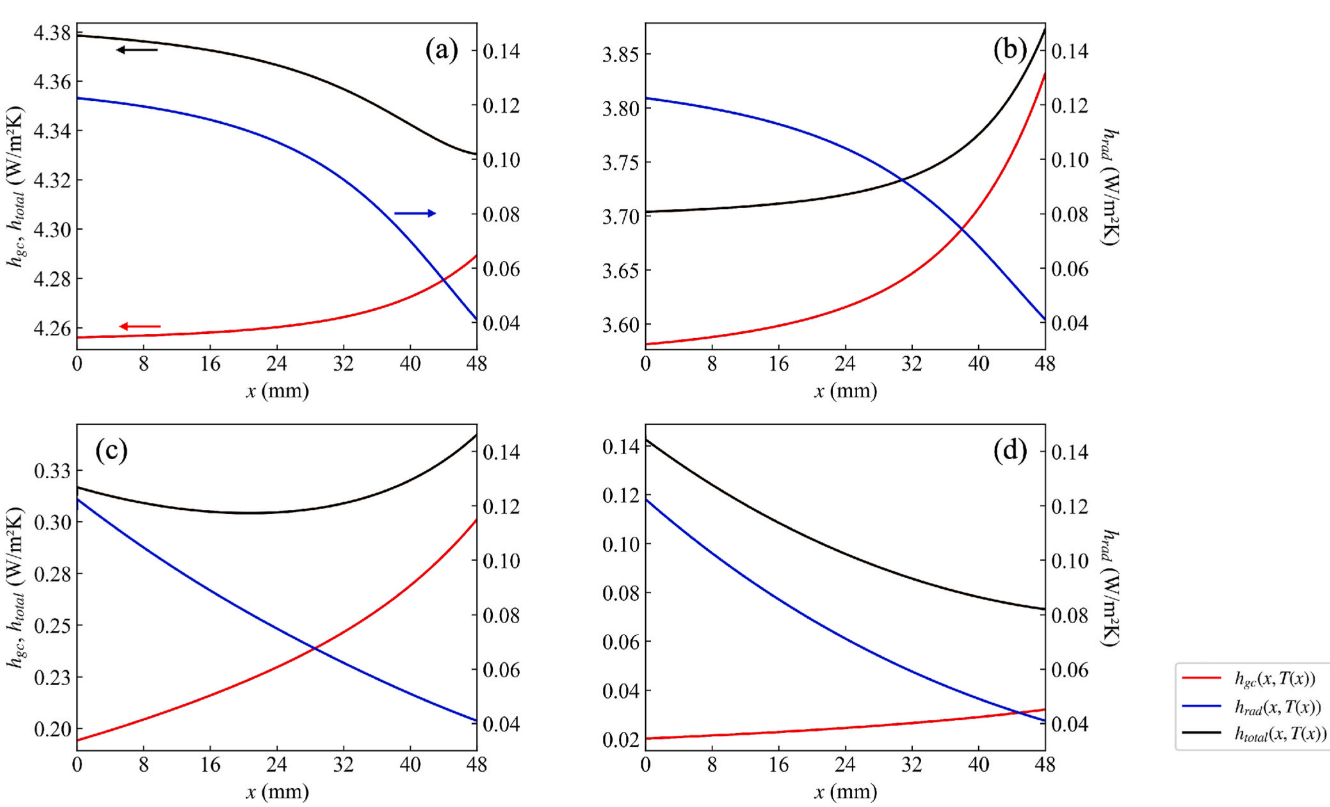

Fig. 13. Spatial variation of the heat transfer coefficients along the cold well under steady-state conditions at different rarefied gas pressures: (a) 1 Torr, (b) 10^{-1} Torr, (c) 10^{-3} Torr, and (d) 10^{-4} Torr.

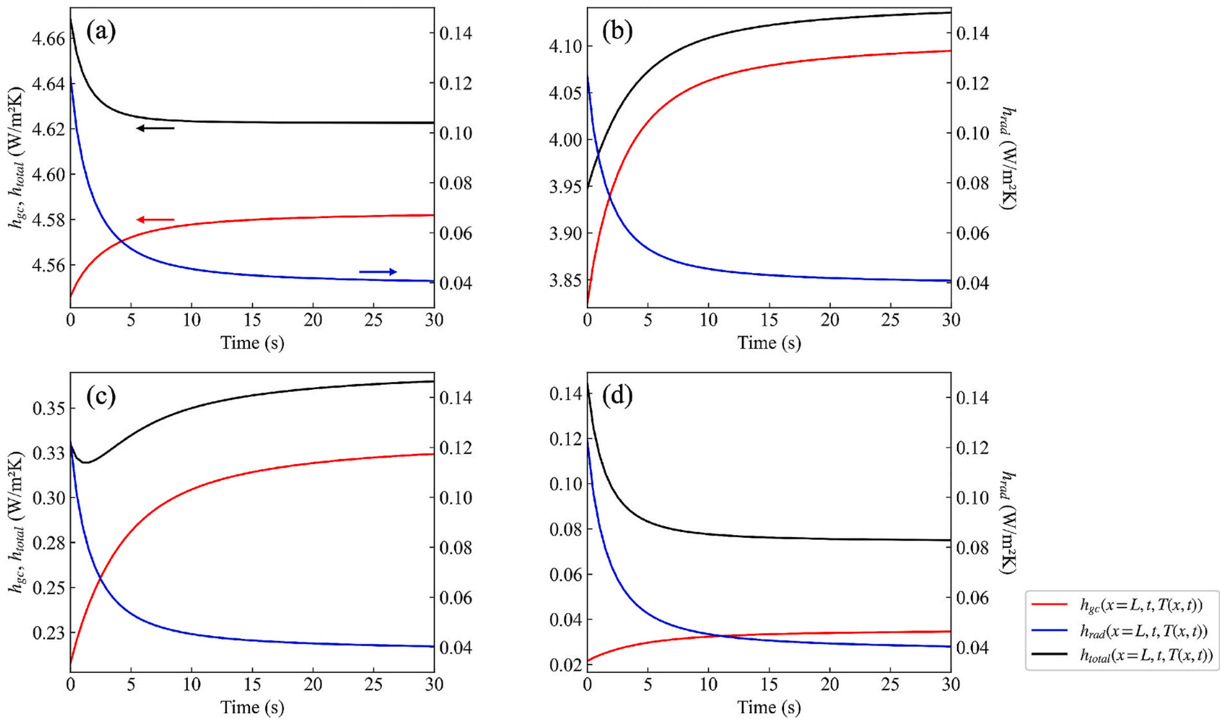

Fig. 14. Temporal variation of heat transfer coefficients at the cold well tip ($x = L$) under transient conditions for different rarefied gas pressures: (a) 1 Torr, (b) 10^{-1} Torr, (c) 10^{-3} Torr, and (d) 10^{-4} Torr.

severely suppressed due to limited molecular interactions, making radiative cooling dominant in the early stages. As the temperature decreases and the radiative term weakens, the overall heat dissipation slows markedly, as reflected by the nearly flat $h_{\text{total}}(x = L, t, T(x,t))$ curve. These results demonstrate that, under transient conditions, the dynamic evolution of temperature substantially alters the relative contributions of gas conduction and radiation. Properly capturing their spatiotemporal dependence is therefore essential for accurately modeling and optimizing cooldown performance in cryogenic systems.

Fig. 15 highlights the spatiotemporal evolution of heat transfer coefficients (h_{gc}, h_{rad}, and h_{total}) based on 2-dimensional contour plots at rarefied gas pressure of 10^{-3} Torr. The rarefied gas heat transfer coefficient that h_{gc} gradually increases along the axial direction and stabilizes over time due to the saturation of thermal gradients. Meanwhile, h_{rad} rapidly decays as the chamber cools, reflecting its strong dependency on high temperatures. The total heat transfer coefficient exhibits a nonlinear interaction between the two modes: it initially decreases due to the dominant drop in h_{gc}, resulting in a concave profile in the spatial–temporal plane. This dynamic behavior emphasizes the importance of capturing both heat transfer modes to accurately model cooling performance when geometrical complexity is additionally involved.

6. Conclusion

This study presents a PINN solution for determining thermal conductance in a cryogenic chamber, with a focus on the effects of rarefied gas conduction and radiative heat transfer. By utilizing both steady-state and transient-state models, the study accurately captures rarefied heat transfer in the cryogenic chamber. The PINN framework incorporates differential equation constraints and boundary conditions into the loss functions, enabling solutions through optimization processes, such as training neural networks. The results demonstrate that solid body conductivity, surface emissivity, and gas pressure significantly influence the cooling load. The transient-state model further highlights the importance of accurately modeling boundary conditions and dynamic thermal properties to reflect real-world scenarios. The use

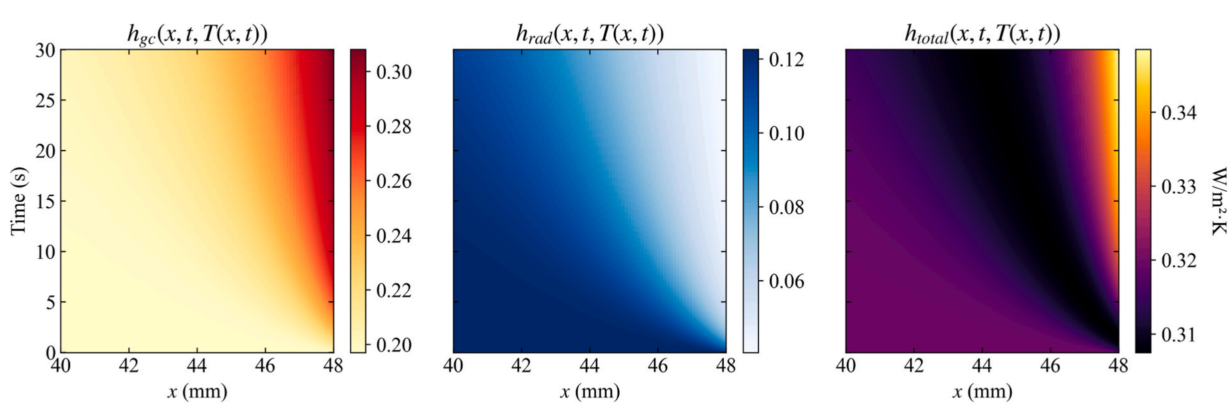

Fig. 15. Spatiotemporal evolution of heat transfer coefficients near the cold tip from 40 to 48 mm along the axial direction. Each panel presents a 2D color map showing how local heat transfer mechanisms vary over both time and position.

of weighted loss functions particularly emphasizes these critical factors.

Additionally, the presented PINN solution is extended to construct an inverse problem solver, aiming to identify material properties or operating conditions that satisfy specific requirements in cryogenic chambers, such as steady cooling load and cooldown time. Example cases include determining the thermal conductivity of the cold well and the rarefied gas pressure in the vessel. The results of the inverse problem solver correspond favorably with those of forward problem simulations across a range of steady cooling loads and cooldown times. These findings suggest that the proposed methodology can not only simulate heat transfer in cryogenic systems, particularly those involving rarefied gas conduction, but also directly optimize material and operating parameters that determine the thermal characteristics of cryogenic systems.

This study assumes idealized boundary conditions and material properties, which may not fully capture the complexities of practical cryogenic systems. Additionally, the focus on one-dimensional heat transfer limits the model's applicability to more complex geometries. A promising future direction is the exploration of inverse problems where the developed models could be used to determine unknown thermal properties or boundary conditions from observed temperature data. This approach has the potential to enhance the design and real-time optimization of cryogenic systems. Extending the models to multidimensional scenarios and incorporating more detailed material properties would further improve their accuracy and applicability. In summary, this work provides a valuable framework for understanding and optimizing cryogenic systems. It not only deepens the understanding of thermal behaviors but also lays the groundwork for future applications, including the potential to solve inverse problems. Such advancements could significantly impact the design and control of advanced cryogenic technologies.

CRediT authorship contribution statement

Sang-Hyun Rhie: Writing – original draft, Validation, Software, Investigation, Formal analysis. **Eric Coatanéa:** Investigation, Formal analysis. **Sanga Lee:** Data curation, Resources. **Wonjong Jung:** Supervision, Investigation, Conceptualization. **Jeongsu Lee:** Writing – review & editing, Investigation, Funding acquisition, Conceptualization.

Declaration of competing interest

The authors declare that they have no known competing financial interests or personal relationships that could have appeared to influence the work reported in this paper.

Acknowledgement

This work was supported by the National Research Foundation of Korea (NRF), funded by the Korean government (MSIT), under Grant No. RS-2023-00279929. It was also supported by the Korea Institute of Industrial Technology (KITECH), under Grant No. EH250001.

Appendix A

Comparative Analysis of CPU and GPU Training

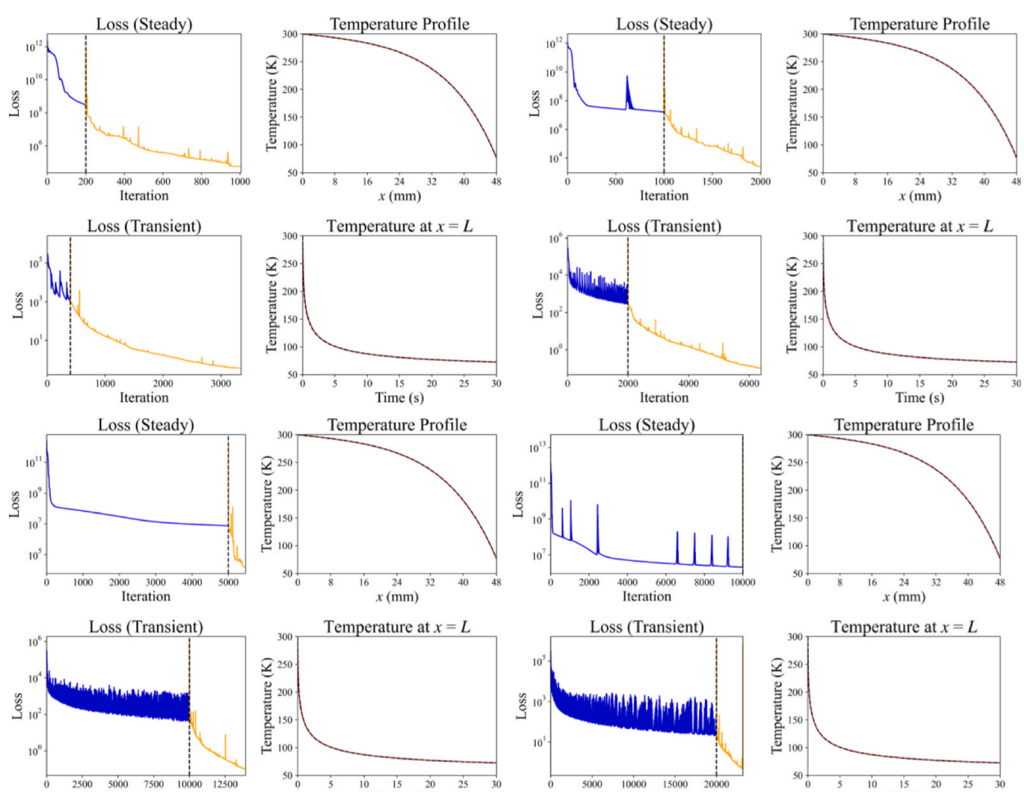

Fig. A1. Results of training loss for steady and transient analyses. The temperature profile along the length and the tip temperature over time are presented for verification. The rows correspond to the following computational conditions: CPU computation with steady-state epochs of 200 and transient-state epochs of 400, followed by steady-state epochs of 1000 and transient-state epochs of 2000, then steady-state epochs of 5000 and transient-state epochs of 10000, and finally steady-state epochs of 10000 and transient-state epochs of 20000.

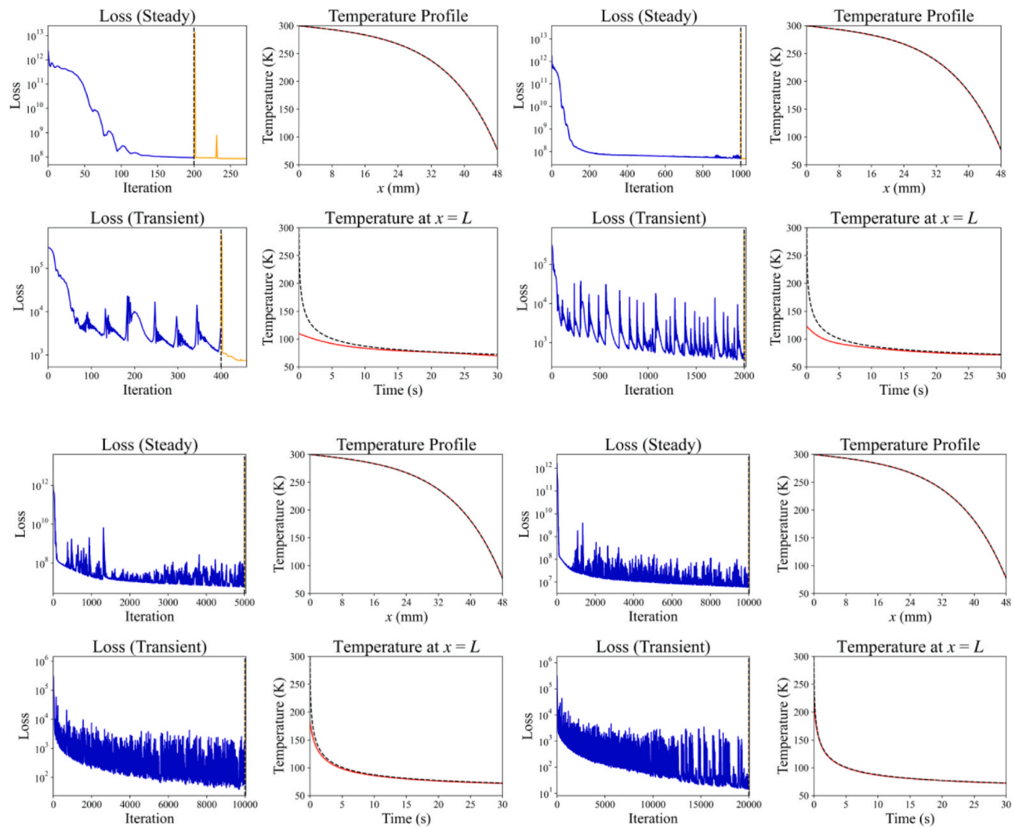

Fig. A2. Results of training loss for steady and transient analyses. The temperature profile along the length and the tip temperature over time are presented for verification. The rows correspond to the following computational conditions: GPU computation with steady-state epochs of 200 and transient-state epochs of 400, steady-state epochs of 1000 and transient-state epochs of 2000, steady-state epochs of 5000 and transient-state epochs of 10000, and steady-state epochs of 10000 and transient-state epochs of 20000.

This appendix presents a brief comparison of the training processes for PINNs using both CPU and GPU computing, along with the observed challenges related to the use of the L-BFGS-B optimizer. The analysis focuses on convergence behavior, efficiency, and potential issues encountered during the training of both steady-state and transient-state models.

CPU-based training tends to be slower due to its sequential processing nature. While the steady-state model can achieve convergence within a reasonable number of epochs, the transient-state model—requiring more complex, time-dependent computations—demands significantly more training iterations. This leads to longer training times on CPU, especially when handling transient dynamics. In contrast, GPU-based training leverages parallel processing, significantly improving efficiency for deep learning tasks like PINNs. The GPU allowed for rapid convergence in the early stages, reducing the overall number of epochs required for the steady-state model. However, the transient-state model on GPU still experienced some instability, with the loss function showing fluctuations, indicating that additional adjustments might be necessary for handling time-dependent complexity.

L-BFGS-B is widely recognized for its precise optimization capabilities. However, during the training process, particularly for the transient-state model, several challenges emerged after transitioning from the Adam optimizer. One of the primary issues was the instability in the loss function, especially with the transient model. This instability likely stems from the inherent complexity of transient heat transfer where the time-dependent nature introduces additional nonlinearities that can complicate the optimization process. As a result, L-BFGS-B struggled to stabilize the loss function effectively.

Another challenge was L-BFGS-B's sensitivity to initial conditions set during the Adam phase. If the Adam optimizer does not sufficiently guide the model toward an optimal state, L-BFGS-B can have difficulty refining the solution further, leading to unpredictable loss behavior. This sensitivity means that the success of L-BFGS-B depends heavily on the quality of the pre-training phase.

Additionally, L-BFGS-B requires full-batch processing, meaning all data points must be considered at once when updating parameters. This can be computationally expensive, particularly for transient-state problems with large datasets. In contrast, optimizers like Adam handle mini-batches more efficiently, which may explain why L-BFGS-B showed instability when processing large amounts of data in one pass.

In both CPU and GPU cases, the GPU required fewer epochs to achieve convergence. However, even with fewer epochs, the transient model on GPU faced challenges, particularly when switching to L-BFGS-B, which highlights that hardware improvements alone do not fully resolve optimization difficulties.

Although GPUs significantly accelerates the training process, the transient-state model encounters inherent challenges, especially when using L-BFGS-B as the optimizer. The oscillations in the loss function and instability in transient problems indicate the need for further refinement of hyperparameters, sampling strategies, and pre-training with Adam. CPUs, while slower, tend to exhibit more stable convergence but require substantially more epochs, particularly for time-dependent models. Resolving issues related to L-BFGS-B, such as its sensitivity to initial conditions and reliance on full-batch updates, could enhance overall training stability.

Data availability

The source codes are available at https://github.com/SHRhie/.

References

[1] Y. Chen, M.A. Serio, S. Sathyamoorthy, Development of a fire detection system using FT-IR spectroscopy and artificial neural networks, Proc. Sixth Int. Symp. Int. Assoc. Fire Saf. Sci. 6 (1999) 791–802, https://doi.org/10.3801/IAFSS.FSS.6-791.
[2] B.U. Töreyin, R.G. Cinbiş, Y. Dedeoğlu, A.E. Çetin, Fire detection in infrared video using wavelet analysis, Opt. Eng. 46 (6) (2007) 067204, https://doi.org/10.1117/1.2748752.
[3] R. Ismail, Z. Omar, S. Suaibun, Obstacle-avoiding robot with IR and PIR motion sensors, IOP Conf. Ser.: Mater. Sci. Eng. 152 (1) (2016) 012064, https://doi.org/10.1088/1757-899X/152/1/012064.
[4] I. Ullah, Q. Ullah, F. Ullah, S. Shin, Sensor-based autonomous robot navigation with distance control, J. Comput. Intell. Electron. Syst. 1 (2) (2012) 161–168, https://doi.org/10.1166/JCIES.2013.1028.
[5] A.N. Huda, S. Taib, Application of infrared thermography for predictive/preventive maintenance of thermal defect in electrical equipment, Appl. Therm. Eng. 61 (2) (2013) 220–227, https://doi.org/10.1016/j.applthermaleng.2013.08.003.
[6] A. Rogalski, HgCdTe infrared detector material: history, status and outlook, Rep. Prog. Phys. 68 (10) (2005) 2267–2336, https://doi.org/10.1088/0034-4885/68/10/R01.
[7] N. Rajic, N. Street, A performance comparison between cooled and uncooled infrared detectors for thermoelastic stress analysis, Quant. Infrared Thermogr. J. 11 (2) (2014) 207–221, https://doi.org/10.1080/17686733.2014.962835.
[8] R. Haj-Ali, B.S. Wei, S. Johnson, R. El-Hajjar, Thermoelastic and infrared-thermography methods for surface strains in cracked orthotropic composite materials, Eng. Fract. Mech. 75 (1) (2008) 58–75, https://doi.org/10.1016/j.engfracmech.2007.02.014.
[9] B.B. Lahiri, S. Bagavathiappan, T. Jayakumar, J. Philip, Medical applications of infrared thermography: a review, Infrared Phys. Technol. 55 (4) (2012) 221–235, https://doi.org/10.1016/j.infrared.2012.03.007.
[10] M. Frize, C. Adéa, P. Payeur, M.D. Gina Di Primio, J. Karsh, A. Ogungbemile, Detection of rheumatoid arthritis using infrared imaging, Med. Imaging 2011: Image Process. 7962 (2011) 205–215, https://doi.org/10.1117/12.874552.
[11] W. Lei, J. Antoszewski, L. Faraone, Progress, challenges, and opportunities for HgCdTe infrared materials and detectors, Appl. Phys. Rev. 2 (4) (2015) 041303, https://doi.org/10.1063/1.4936577.
[12] H.Y. Kim, B.H. Kang, D.Y. Lee, A parametric study on the cooling characteristics of an infrared detector cryochamber, Cryogenics 40 (12) (2000) 779–788, https://doi.org/10.1016/S0011-2275(01)00033-9.
[13] M. Fassin, D. Kowollik, S. Wulfinghoff, S. Reese, M. Haupt, Design studies of rocket engine cooling structures for fatigue experiments, Arch. Appl. Mech. 86 (2016) 2063–2093, https://doi.org/10.1007/s00419-016-1160-6.
[14] X. Dong, D. Sun, C. Wang, Q. Shen, Y. Duan, Numerical study on cryogenic distillation process for producing high-purity methane from LNG with LNG exergy utilization, Appl. Therm. Eng. 262 (2025) 125203, https://doi.org/10.1016/j.applthermaleng.2024.125203.
[15] L. Wang, Z. Chen, H. Meng, Numerical study of conjugate heat transfer of cryogenic methane in rectangular engine cooling channels at supercritical pressures, Appl. Therm. Eng. 54 (1) (2013) 237–246, https://doi.org/10.1016/j.applthermaleng.2013.02.007.
[16] J.M. Pfotenhauer, X. Sun, A. Berryhill, C.B. Shoemaker, The influence of aspect ratio on the thermal performance of a cryogenic pulsating heat pipe, Appl. Therm. Eng. 196 (2021) 117322, https://doi.org/10.1016/j.applthermaleng.2021.117322.
[17] M. Singhal, G. Singhal, A.C. Verma, S. Kumar, M. Singh, Thermophysics modeling of an infrared detector cryochamber for transient operational scenario, Infrared Phys. Technol. 76 (2016) 103–110, https://doi.org/10.1016/j.infrared.2016.01.023.
[18] C. Yuan, Z. Liu, Y. Zhang, Fire detection using infrared images for UAV-based forest fire surveillance, in: Proc. 2017 Int. Conf. Unmanned Aircraft Syst. (ICUAS), IEEE, 2017, pp. 567–572, https://doi.org/10.1109/ICUAS.2017.7991306.
[19] B.H. Kim, Thermal analysis of a cryochamber for an infrared detector considering a radiation shield, Korean J. Air-Cond. Refrig. Eng. 18 (8) (2006) 672–677.
[20] E.C. Luo, Y. Zhou, M.Q. Gong, Thermodynamic analysis and optimization of 80 K closed-cycle Joule–Thompson cryocooler with gas mixture, Adv. Cryog. Eng. (1998) 1679–1683, https://doi.org/10.1007/978-1-4757-9047-4_211.
[21] M.D. Atrey. Cryocooler technology: The path to invisible and reliable cryogenics, in: Cryocoolers: Theory and Applications, Springer (2020) 1–46. https://doi.org/10.1007/978-3-030-11307-0_1.
[22] T. Shimazaki, K. Toyoda, A. Oota, H. Nozato, T. Usuda, O. Tamura, Closed-cycle Joule–Thomson cryocooler for resistance thermometer calibration down to 0.65 K, Int. J. Thermophys. 29 (1) (2008) 42–50, https://doi.org/10.1007/s10765-007-0341-5.
[23] R. Radebaugh, P. Bradley, C. Coolidge, R. Lewis, Y.C. Lee, Design and analysis of a 150 K cascade Joule–Thomson microcooler, Cryocoolers 18 (2014) 377–388, https://doi.org/10.1109/ICMREE.2011.5930561.
[24] J. Yu, Improving the performance of small Joule–Thomson cryocooler, Cryogenics 48 (9–10) (2008) 426–431, https://doi.org/10.1016/j.cryogenics.2008.05.006.
[25] M. Singhal, G. Singhal, A.C. Verma, S. Kumar, M. Singh, Numerical investigation of steady-state thermal behavior of an infrared detector cryo chamber, Therm. Sci. 21 (3) (2017) 1203–1212, https://doi.org/10.2298/TSCI140617107S.
[26] M. Singhal, R. Kumar, R.S. Walia, S.K. Pandey, Experimental investigation and thermophysics analysis of Joule–Thomson cooler applicable to infrared imaging, Def. Sci. J. 73 (4) (2023), https://doi.org/10.14429/dsj.73.18686.
[27] A. Veprik, S. Zehtzer, H. Vilenchik, N. Pundak, Micro-miniature split Stirling linear cryocooler, AIP Conf. Proc. 1218 (1) (2010) 363–370, https://doi.org/10.1063/1.3422375.
[28] J. Yan, Z. Liu, Z. Liu, Y. Wang, D. Wang, L. Shen, A performance degradation and lifetime prediction model for thermoelectric device under thermal cycling, Appl. Therm. Eng. 228 (2025) 126655, https://doi.org/10.1016/j.applthermaleng.2025.126655.
[29] L. Zhou, F. Meng, Y. Sun, Numerical study on infrared detectors cooling by multi-stage thermoelectric cooler combined with microchannel heat sink, Appl. Therm. Eng. 236 (2024) 121788, https://doi.org/10.1016/j.applthermaleng.2023.121788.
[30] M. Raissi, P. Perdikaris, G.E. Karniadakis, Physics-informed neural networks: a deep learning framework for solving forward and inverse problems involving nonlinear partial differential equations, J. Comput. Phys. 378 (2019) 686–707, https://doi.org/10.1016/j.jcp.2018.10.045.
[31] G. Engel. Neural networks to approximate solutions of ordinary differential equations, in: Proc. Int. Conf. Mach. Learn., 2019, pp. 208–228. https://doi.org/10.1007/978-3-030-22871-2_54.
[32] N. Zobeiry, W. Lee, A physics-informed machine learning approach for solving heat transfer equation in advanced manufacturing and engineering applications, Eng. Appl. Artif. Intell. 101 (2020) 104232, https://doi.org/10.1016/j.engappai.2021.104232.
[33] N.Z. Dhamirah Mohamad, A. Yousif, N.A.B. Shaari, H.I. Mustafa, S.A. Abdul Karim, A. Shafie, M. Izzatullah, Heat transfer modelling with physics-informed neural network (PINN), in: Intelligent Systems Modeling and Simulation II, Springer Int. Publ., 2022, pp. 25–35. DOI: https://doi.org/10.1007/978-3-031-04028-3_3.
[34] Y. Wang, Q. Ren, A versatile inversion approach for space/temperature/time-related thermal conductivity via deep learning, Int. J. Heat Mass Transf. 186 (2022) 122444, https://doi.org/10.1016/j.ijheatmasstransfer.2021.122444.
[35] X. Zhao, K. Shirvan, R.K. Salko, F. Guo, On the prediction of critical heat flux using a physics-informed machine learning-aided framework, Appl. Therm. Eng. 164 (2020) 114540, https://doi.org/10.1016/j.applthermaleng.2019.114540.
[36] S. Cai, Z. Wang, S. Wang, P. Perdikaris, G.E. Karniadakis, Physics-informed neural networks for heat transfer problems, J. Heat Transf. 143 (6) (2021) 060801, https://doi.org/10.1115/1.4050542.
[37] W. Wang, B. Yu, Q. Ai, M. Liu, Y. Shuai, X. Wang, X. Zhang, Reconstructing 3D temperature fields from sparse discrete data by analytical solution-embedded neural network, Appl. Therm. Eng. 264 (2025) 125448, https://doi.org/10.1016/j.applthermaleng.2025.125448.
[38] V.S. Arpaci, Conduction Heat Transfer, Addison-Wesley, 1966.
[39] F. Sharipov, Rarefied Gas Dynamics: Fundamentals for Research and Practice, John Wiley & Sons, 2015.
[40] R.D. Zucker, O. Biblarz, Fundamentals of Gas Dynamics, John Wiley & Sons, 2019.
[41] R.D. Present, Kinetic Theory of Gases, McGraw-Hill, 1958.
[42] M.F. Modest, S. Mazumder, Radiative Heat Transfer, Academic Press, 2021.
[43] J. Lee, Anti-derivatives approximator for enhancing physics-informed neural networks, Comput. Methods Appl. Mech. Eng. 426 (2024) 117000, https://doi.org/10.1016/j.cma.2024.117000.
[44] D.P. Kingma, J. Ba. Adam: A method for stochastic optimization, arXiv preprint arXiv:1412.6980 (2014). DOI: https://doi.org/10.48550/arXiv.1412.6980.
[45] C. Zhu, R.H. Byrd, P. Lu, J. Nocedal, Algorithm 778: L-BFGS-B: Fortran subroutines for large-scale bound-constrained optimization, ACM Trans. Math. Softw. 23 (4) (1997) 550–560, https://doi.org/10.1145/279232.279236.
[46] H.S. Carslaw, J.C. Jaeger, Conduction of Heat in Solids, Clarendon Press, 1959.
[47] M. Baldan, P. Di Barba, D.A. Lowther, Physics-informed neural networks for inverse electromagnetic problems, IEEE Trans. Magn. 59 (5) (2023) 1–5, https://doi.org/10.1109/TMAG.2023.3247023.
[48] T. Kadeethum, T.M. Jørgensen, H.M. Nick. Physics-informed neural networks for solving inverse problems of nonlinear Biot's equations: Batch training, ARMA US Rock Mech./Geomech. Symp. (2020). DOI: https://doi.org/10.48550/arXiv.2005.09638.
[49] A.D. Jagtap, Z. Mao, N. Adams, G.E. Karniadakis, Physics-informed neural networks for inverse problems in supersonic flows, J. Comput. Phys. 466 (2022) 111402, https://doi.org/10.1016/j.jcp.2022.111402.
[50] C. Yan, Y. Zhang, J. Qiu, Y. Chen, X. Wang, W. Dai, M. Ma, H. Li, E. Luo, Numerical and experimental study of partly tapered pulse tube in a pulse tube cryocooler, Int. J. Refrig. 120 (2020) 474–480, https://doi.org/10.1016/j.ijrefrig.2020.09.013.
[51] C. Escriba, E. Campo, D. Esteve, J.Y. Fourniols, Complete analytical modeling and analysis of micromachined thermoelectric uncooled IR sensors, Sens. Actuators A Phys. 120 (267–276) (2005) 267–276, https://doi.org/10.1016/j.sna.2004.11.027.